Publikation Nr 97/1
ISSN 1101-9972

ISRN CTH-TFD-PB-97/1-SE

CHALMERS TEKNISKA HÖGSKOLA
Institutionen för Termo- och Fluiddynamik

CHALMERS UNIVERSITY OF TECHNOLOGY
Department of Thermo and Fluid Dynamics

Reynolds Stress Modeling of Flow Separation on Curved Surfaces.

by

Sven Perzon

Thesis for the degree of Licentiate of Engineering

Göteborg, May 1997

Abstract

Several Reynolds stress models were used in a well-validated, commercial Computational Fluid Dynamics software. The models were tested on two-dimensional and three-dimensional "industrial-like" test cases. The Reynolds stress models generally give more accurate results than eddy viscosity models, although the differences are in many cases marginal. Design parameters such as drag are often predicted poorly even when a Reynolds stress model is used. Eddy viscosity models are surprisingly accurate, even when the simulated flow includes complex physics, see Ramnefors *et al.* [30], [31].

Reynolds stress models are poorer than eddy viscosity models in terms of numerical stability. No natural diffusion stabilizer is present in the momentum equations, and thus some special treatment must be imposed. Even so, the stability properties of a system of equations emanating from the use of a Reynolds stress model are worse than those that emerge when using an eddy viscosity model is used. In many situations, this fact leads to divergence when using a Renolds stress model. This is especially true in 3D, where severe stability problems have been encountered. Low Reynolds number RSMs are impossible to use in many flow situations and, thus, the usage is limited to wall-function-based models or two-layer models.

As the wall boundary conditions have been proven to be very important, a realizable low Reynolds number RSM has been proposed in an attempt to solve part of the stability problems, since the corresponding high Reynolds number model by Launder and Li [22] showed some potential. Unfortunately this model still suffers from stability problems.

The accuracy achieved by the Reynolds stress model in comparison with an eddy viscosity model is not sufficiently large to excuse the troublesome numerical behaviour of the equations. Unless any new numerical feature is proposed, Reynolds stress models will probably not be used widely in industry.

Acknowledgment

I am greatful to Prof. Lars Davidson and Dr. Mats Ramnefors for their supervision and support throughout the course of this study. I also appreciate the cooperation of Dr. Magnus Hallbäck from the Royal Institute of Technology in Stockholm. Collaboration with AEA CFDS, Harwell Laboratories in Oxfordshire has been very fruitful and, thus, I extend my great thanks to Nigel Wilkes, Alain Burns, Suzanne Simcox and others working at AEA, for their great support. Many thanks also to the staff at the department of Thermo and Fluiddynamics, Chalmers University of Technology, and to the staff of Volvo Data AB for their assistance and guidance. An extra thanks to the Chalmers administrators, Monika, Ulla and Birgitta who have been wonderful.

This study was funded by NUTEK and its "Ramprogram för strömningsteknik". The computer resources were provided by Chalmers University of Technology and Volvo Data AB.

Contents

Chapter 1

Introduction

When simulating almost any external flow of technical interest there is a curved boundary present. The curvature is important in terms of boundary layer development and turbulence. Many of the turbulence models available in CFD codes today poorly predict these curvature effects. Eddy Viscosity Models (EVM) predict curvature effects incorrectly. Second-order closures, e.g. Reynolds Stress Models (RSM), do account for streamline curvature and should mimic the turbulence more accurately under these circumstances. However, even with the use of RSMs, the location of the separation point/line, for instance, is not sufficiently accurate, which in turn significantly affects the accuracy of e.g. drag predictions. The aim of this project was thus to increase the understanding of how Reynolds stress turbulence models perform in advanced industrial flows such as those that include separation and streamline curvatures. Additional models are implemented in the commercial CFD software, CFX4, [3], formerly CFDS-FLOW3D from AEA Technology, Harwell Laboratories, UK. AEA has made relevant parts of the code available for this study. Evaluations have been made in cooperation with Volvo Data AB, where the models have also been tested in an industrial environment.

Chapter 2

Turbulence models

This chapter briefly introduces the reader to the turbulence models used in this study. Some thought is taken from basic physical relations and, thus requiring a brief introduction to such relations. The relations below can be found in all textbooks on the topic, such as Tennekes and Lumley [34], who give more rigourous explanations and derivations.

2.1 Basic relations

Starting from the Navier Stokes equations for an incompressible flow,

$$\frac{Du_i}{Dt} = -\frac{1}{\rho}\frac{\partial p}{\partial x_i} + \frac{\partial}{\partial x_j}\left(\nu\frac{\partial u_i}{\partial x_j}\right) \tag{2.1}$$

$$\frac{\partial u_i}{\partial x_i} = 0 \tag{2.2}$$

one can use the Reynolds decomposition in which the velocity and pressure are split into a time-averaged mean part, U_i P, and a fluctuating part, u_i' p', that is

$$\begin{aligned} u_i &= U_i + u_i' \\ p &= P + p' \end{aligned} \tag{2.3}$$

Perform a time average of equation (2.1) to obtain the Reynolds equation.

$$\frac{DU_i}{Dt} = -\frac{1}{\rho}\frac{\partial P}{\partial x_i} + \frac{\partial}{\partial x_j}\left(\nu\frac{\partial U_i}{\partial x_j} - \overline{u_i u_j}\right) \tag{2.4}$$

$$\frac{\partial U_i}{\partial x_i} = 0 \tag{2.5}$$

The $\overline{u_i u_j}$ are the additive unknown Reynolds stresses which in turn must be solved or modeled. It is possible to derive exact relations for the Reynolds stresses, see [34],

$$\frac{D\overline{u_i u_j}}{Dt} = \underbrace{-\left(\overline{u_i u_k}\frac{\partial U_j}{\partial x_k} + \overline{u_j u_k}\frac{\partial U_i}{\partial x_k}\right)}_{P_{ij}}$$

$$\underbrace{-\frac{\partial}{\partial x_k}\left(\overline{u_i u_j u_k}+\frac{\overline{pu_j}}{\rho}\delta_{jk}+\frac{\overline{pu_i}}{\rho}\delta_{ik}\right)}_{d_{ij}^t}\underbrace{-\frac{\partial}{\partial x_k}\left(-\nu\frac{\partial\overline{u_i u_j}}{\partial x_k}\right)}_{d_{ij}^v}$$
$$+\underbrace{\overline{\frac{p}{\rho}\left(\frac{\partial u_i}{\partial x_j}+\frac{\partial u_i}{\partial x_j}\right)}}_{\phi_{ij}}-\underbrace{2\nu\overline{\frac{\partial u_i}{\partial x_k}\frac{\partial u_j}{\partial x_k}}}_{\varepsilon_{ij}} \tag{2.6}$$

The terms on the right-hand side can be identified as production, P_{ij}, turbulent diffusion, d_{ij}^t, viscous diffusion, d_{ij}^v, pressure strain interaction, ϕ_{ij}, and dissipation, ε_{ij}. The production term, P_{ij}, and the viscous diffusion term, d_{ij}^v, are exact. However, more unknowns are introduced and modeling is thus needed. Taking half the trace of equation (2.6) gives an equation for the turbulent kinetic energy, $k \equiv \frac{1}{2}\overline{u_i u_i}$

$$\frac{Dk}{Dt} = \underbrace{-\overline{u_i u_j}\left(\overbrace{\frac{1}{2}\left(\frac{\partial U_i}{\partial x_j}+\frac{\partial U_j}{\partial x_i}\right)}^{S_{ij}}\right)}_{P_k}-\underbrace{\nu\overline{\frac{\partial u_i}{\partial x_j}\frac{\partial u_i}{\partial x_j}}}_{\varepsilon}$$
$$\underbrace{-\frac{\partial}{\partial x_j}\left(\frac{1}{2}\overline{u_i u_j u_k}+\frac{\overline{pu_j}}{\rho}\right)}_{d_k}\underbrace{-\frac{\partial}{\partial x_j}\left(-\nu\frac{\partial k}{\partial x_j}\right)}_{d_v} \tag{2.7}$$

The terms on the right-hand side are interpreted as production (P_k), dissipation (ε), turbulent diffusion (d_k) and viscous diffusion (d_v). S_{ij} is the mean strain rate tensor. All terms except the viscous diffusion term usually need to be modeled. The production term is exact whenever

the Reynolds stresses are available. The transport equation for the dissipation rate, ε, can be written, see [16],

$$\frac{D\varepsilon}{Dt} = \mathcal{P}^{\varepsilon 1}+\mathcal{P}^{\varepsilon 2}+\mathcal{P}^{\varepsilon 3}+T^{\varepsilon}-D^{\varepsilon}-\frac{\partial}{\partial x_m}\left(J_m^{\varepsilon}-\nu\frac{\partial\varepsilon}{\partial x_m}\right) \tag{2.8}$$

where

$$\mathcal{P}^{\varepsilon 1} = -2\nu S_{ij}\overline{\frac{\partial u_i'}{\partial x_k}\frac{\partial u_j'}{\partial x_k}}$$
$$\mathcal{P}^{\varepsilon 2} = -2\nu S_{ij}\overline{\frac{\partial u_k'}{\partial x_i}\frac{\partial u_k'}{\partial x_j}}$$
$$\mathcal{P}^{\varepsilon 3} = -2\nu\frac{\partial^2 U_i}{\partial x_j\partial x_k}\overline{u_j'\frac{\partial u_i'}{\partial x_k}}$$
$$T^{\varepsilon} = -2\nu\overline{\frac{\partial u_i'}{\partial x_j}\frac{\partial u_i'}{\partial x_k}\frac{\partial u_j'}{\partial x_k}}$$
$$D^{\varepsilon} = 2\nu^2\overline{\frac{\partial^2 u_i'}{\partial x_j\partial x_k}\frac{\partial^2 u_i'}{\partial x_j\partial x_k}}$$

$$J_m^\varepsilon = \nu \left(\overline{\frac{\partial u_i'}{\partial x_j} \frac{\partial u_i'}{\partial x_j} u_m'} + \frac{2}{\rho} \overline{\frac{\partial p'}{\partial x_i} \frac{\partial u_m'}{\partial x_i}} \right)$$

The terms can be identified as production related to the mean flow ($\mathcal{P}^{\varepsilon i}$ $i = 1..3$), production related to turbulence (T^ε), viscous destruction (D^ε), turbulent diffusion (J_m^ε) and viscous diffusion ($-\nu \partial \varepsilon / \partial x_m$). Models are needed for all terms but the viscous diffusion term.

All equations described above are exact but new unknowns are incorporated into the problem, thus requiring models. In eddy viscosity models modeling already begins in the Reynolds equations, (2.4-2.5), by a model for the Reynolds stresses that emanates as additive unknowns in the equations. For this matter, two scalar equations are used for computing an eddy viscosity, which in turn is used in the model of the Reynolds stresses. The scalars are usually the turbulent kinetic energy, k, together with the eddy dissipation rate, ε.

Reynolds stress models do not encounter any modeling of the terms in the Reynolds equations, (2.4-2.5), since the Reynolds stresses are solved for. The modeling is instead directed toward the stress equation and the complementary scalar equation. The most widely used scalar in RSMs is the eddy dissipation rate, ε.

2.2 Eddy viscosity models

This study is focused on RSMs, and EVMs are used solely for comparison reasons.The commercial code CFX4 [3] was used throughout this study. Several turbulence models are available in this code, and the models that have been used for comparison are summarized as follows:

- The standard k-ε model by Launder and Spalding [25]. This is a high Reynolds number model and uses wall functions at walls.
- The k-ε model by Launder and Sharma [24]. This low Reynolds number model allows an integration through the boundary layer all the way to the wall.

The two-layer approach by Chen and Patel [7] was also coded and used in this study.

2.2.1 The standard k-ε model.

The standard k-ε model is the most widely used model in industrial applications. The main reason for its popularity is that it is a very numerically robust model. It is also surprisingly accurate for many industrial applications. The model and all other EVMs are built upon the Boussinesq [6] hypothesis,

$$-\overline{u_i u_j} = \nu_t \left(\frac{\partial U_i}{\partial x_j} + \frac{\partial U_j}{\partial x_i} \right) - \frac{2}{3} k \delta_{ij} \tag{2.9}$$

By dimensional analysis, the eddy viscosity can be formulated according to

$$\nu_t = c_\mu \frac{k^2}{\varepsilon} \tag{2.10}$$

The transport equations for k, equation (2.7), and ε, equation (2.8), are simplified to

$$\frac{Dk}{Dt} = P_k - \varepsilon + \frac{\partial}{\partial x_j}\left(\left(\nu + \frac{\nu_t}{\sigma_k}\right)\frac{\partial k}{\partial x_j}\right) \tag{2.11}$$

$$\frac{D\varepsilon}{Dt} = c_{\varepsilon 1}\frac{\varepsilon}{k}P_k - c_{\varepsilon 2}\frac{\varepsilon^2}{k} + \frac{\partial}{\partial x_j}\left(\left(\nu + \frac{\nu_t}{\sigma_\varepsilon}\right)\frac{\partial \varepsilon}{\partial x_j}\right) \tag{2.12}$$

where

$$P_k = \nu_t\left(\frac{\partial U_i}{\partial x_j} + \frac{\partial U_j}{\partial x_i}\right)\frac{\partial U_i}{\partial x_j}$$

Standard values for the model constants are:

$$c_\mu = 0.09 \quad c_{\varepsilon 1} = 1.44 \quad c_{\varepsilon 2} = 1.92 \quad \sigma_k = 1.0 \quad \sigma_\varepsilon = 1.3$$

Wall functions for the k-ε model.

Wall functions are used at the walls. Consider a control volume according to figure 2.1. Quantities evaluated at P are subscripted by a P and quantities evaluated at the wall by W. The turbulent kinetic energy is solved for at the node adjacent to the wall, and the value of the wall shear stress may be evaluated from k_P. A special treatment of the source term in the k equation is needed in order to use quantities from the interior of the flow and already specified boundary conditions on the velocities, see [3]. Furthermore, the momentum flux through the wall is set to zero by the matrix coefficient at the wall, $a_W = 0$. An alternative approach is to fix k at the node adjacent to the wall according to

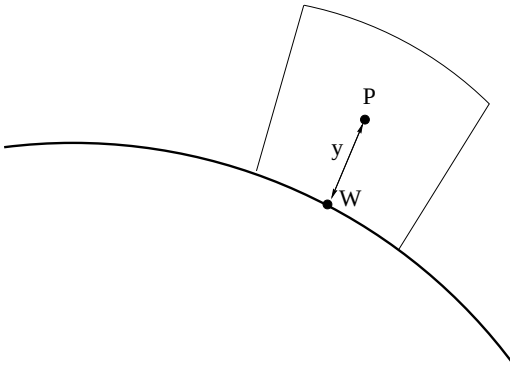

Figure 2.1: *Node adjacent to the wall.*

$$k_P = c_\mu^{-1/2}U^* \tag{2.13}$$

where U^* is taken from the log law

$$\frac{U_P}{U^*} = \frac{1}{\kappa}\ln(Ey^+) \tag{2.14}$$

$$\kappa = 0.4187 \qquad E = 9.793 \tag{2.15}$$

The eddy dissipation rate, ε, is fixed at the node adjacent to the wall in both approaches by the relation

$$\varepsilon_P = \frac{k_P^{3/2}c_\mu^{3/4}}{\kappa y} \tag{2.16}$$

2.2.2 Low Reynolds number k-ε model.

The Launder and Sharma, [24], low Reynolds number k-ε model is one of the most widely used low Reynolds number k-ε models. The equations from the standard model described above are modified in order to work in the near-wall region.

$$\nu_t = c_\mu f_\mu \frac{k^2}{\varepsilon} \tag{2.17}$$

The damping function, f_μ, is expressed as

$$f_\mu = \exp\left(\frac{-3.4}{(1+R_T/50)^2}\right)$$

The transport equation for k is

$$\frac{Dk}{Dt} = P_k - \varepsilon + \frac{\partial}{\partial x_j}\left(\left(\nu + \frac{\nu_t}{\sigma_k}\right)\frac{\partial k}{\partial x_j}\right) \tag{2.18}$$

A transport equation for $\tilde{\varepsilon} \equiv \varepsilon - 2\nu(\partial\sqrt{k}/\partial x_i)^2$ is solved for

$$\frac{D\tilde{\varepsilon}}{Dt} = c_{\varepsilon 1}\frac{\tilde{\varepsilon}}{k}P_k - c_{\varepsilon 2}f_2\frac{\tilde{\varepsilon}^2}{k} + \mathcal{G} + \frac{\partial}{\partial x_j}\left(\left(\nu + \frac{\nu_t}{\sigma_\varepsilon}\right)\frac{\partial \tilde{\varepsilon}}{\partial x_j}\right) \tag{2.19}$$

where the damping function is

$$f_2 = 1 - 0.3\exp(-R_T^2)$$

and the additive source term is

$$\mathcal{G} = 2\nu\nu_t\left(\frac{\partial^2 U_i}{\partial x_j \partial x_k}\right)^2$$

Wall boundary conditions

Since this model allows for the integration of the boundary layer all the way to the wall, the no-slip boundary condition is valid. Velocities and the turbulent kinetic energy is set to zero at the wall. This is also true for the $\tilde{\varepsilon}$ which, contrary to ε, will go to zero when the wall is approached.

2.2.3 Two layer k-ε model.

A two-layer model separates the flow into two regions, one part in the fully turbulent region where the standard k-ε model is valid and the second part in the near-wall region where a one-equation model by Wolfshtein [35] is used. In the near-wall region, the k equation is solved for using a modified eddy viscosity, and the dissipation rate term is modeled by an algebraic relation, see Chen and Patel [7]. The eddy viscosity and the dissipation rate term are

$$\nu_t = c_\mu \sqrt{k} l_\mu \qquad \varepsilon = \frac{k^{3/2}}{l_\varepsilon} \tag{2.20}$$

The length scales are prescribed according to

$$l_\varepsilon = c_l y \left(1 - \exp(-y^*/A_\varepsilon)\right) \qquad l_\mu = c_l y \left(1 - \exp(-R_n/A_\mu)\right) \tag{2.21}$$

where

$$y^* = \sqrt{k} y/\nu \qquad A_\varepsilon = 2c_l \qquad A_\mu = 70 \qquad c_l = \kappa c_\mu^{-3/4}$$

and y is the normal distance to the wall. The one-equation model is applied near the walls for $y^* < 250$.

Wall boundary conditions

This model also allows for the no-slip boundary condition on the velocities and the turbulent kinetic energy. No wall boundary condition is needed for the dissipation rate, since the one-equation model is used in this region.

2.3 Reynolds stress models

Second-moment closures are the main topic of this study, and several models have been implemented and tested in the CFD code, CFX4. There are many models available in the literature and selected models will be presented below. The exact equation for the Reynolds stresses is of course used as a starting point for all models and can be rewritten symbolically according to,

$$\frac{D\overline{u_i u_j}}{Dt} = P_{ij} + d^t_{ij} + d^v_{ij} + \phi_{ij} - \varepsilon_{ij} \tag{2.22}$$

The exact terms are shown in equation (2.6) and can be interpreted as, on the left-hand side, convection, and, on the right-hand side, production, turbulent diffusion, viscous diffusion, pressure strain interaction and dissipation. All terms must be modeled except for the convection, production and viscous diffusion terms, which are exact. The turbulent diffusion term is modeled using the generalized gradient hypothesis by Daly and Harlow [12], that is:

$$d^t_{ij} = \frac{\partial}{\partial x_k}\left(c_s \frac{k}{\varepsilon}\overline{u_k u_l}\frac{\partial \overline{u_i u_j}}{\partial x_l}\right) \tag{2.23}$$

where the constant $c_s = 0.22$. The naming convention of the Reynolds stress models is usually based on the proposed model for the pressures strain interaction term, and the models used in this work can be summarized as follows:

- A combination of the linear return to isotropy term by Rotta [32] and the linear Isotropization of Production term by Naot *et al.* [28]. This model is hereafter named IP in this study.
- The wall reflection terms proposed by Gibson and Launder [15] are used together with the IP model, and the combination is hereafter named GL.
- A non-linear proposal by Speziale, Sarkar and Gatski [33] is used. This model will be referred to as the SSG model.

- The linear model, adapted for low Reynolds number near-wall regions, proposed by Hanjalić and Launder [17], is used. The model will be called HL.
- A cubic proposal by Craft [10] has been used with constants according to Launder and Li [22] and thus is hereafter named LLI.
- The last model used is a mix between the LLI model and the HL model and is referred to as the Present model.

2.3.1 The Isotropization of Production model

As stated above, this IP model is a combination of the return-to-isotropy term by Rotta [32], $\phi_{ij,1}$, and the isotropization of production term by Naot *et al.* [28], $\phi_{ij,2}$,

$$\phi_{ij} = \underbrace{-c_1 \frac{\varepsilon}{k}\left(\overline{u_i u_j} - \frac{2}{3}\delta_{ij}k\right)}_{\phi_{ij,1}} \underbrace{-c_2\left(P_{ij} - \frac{2}{3}\delta_{ij}P_k\right)}_{\phi_{ij,2}} \tag{2.24}$$

where $P_k = \frac{1}{2}P_{ii}$ and the constants take the values proposed in Launder *et al.* [23], that is,

$$c_1 = 1.8 \qquad c_2 = 0.6$$

This model has no wall reflection terms and will thus not properly mimic the turbulence close to a wall.

Since this is a high Reynolds number model, the dissipation tensor is modeled using the assumption that the small scales are isotropic in character and thus

$$\varepsilon_{ij} = \frac{2}{3}\varepsilon\delta_{ij} \tag{2.25}$$

The dissipation equation is solved for in the following form:

$$\frac{D\varepsilon}{Dt} = c_{\varepsilon 1}\frac{\varepsilon}{k}P_k - c_{\varepsilon 2}\frac{\varepsilon^2}{k} + \frac{\partial}{\partial x_i}\left(\left(\nu + \frac{c_s k\overline{u_i u_j}}{\varepsilon\sigma_\varepsilon}\right)\frac{\partial\varepsilon}{\partial x_j}\right) \tag{2.26}$$

Note the differences in comparison with equation (2.12). The diffusion term is generalized, and the production, $P_k = \frac{1}{2}P_{ii}$, is more accurately described using a RSM.

Wall functions for high Reynolds number RSMs

Wall functions are used at the wall boundaries, and the Reynolds stresses are handled according to the proposal of Lien and Leschziner [27], extended to three dimensions. The dissipation rate is set as $\varepsilon = U_*^3/(\kappa y)$ at the node adjacent to the wall. Furthermore, the stresses are set in a local stream aligned coordinate system with unit base vectors $\vec{t} = (t_x, t_y, t_z)$ and $\vec{n} = (n_x, n_y, n_z)$, where $\vec{n}$ is the unit wall normal vector and $\vec{t}$ is the unit wall tangential vector that is aligned with the flow, see figure 2.2. The third component in this orthogonal set of base vectors is taken as the cross-product of $\vec{t}$ and $\vec{n}$. The stresses in this locally symmetric flow are set according to

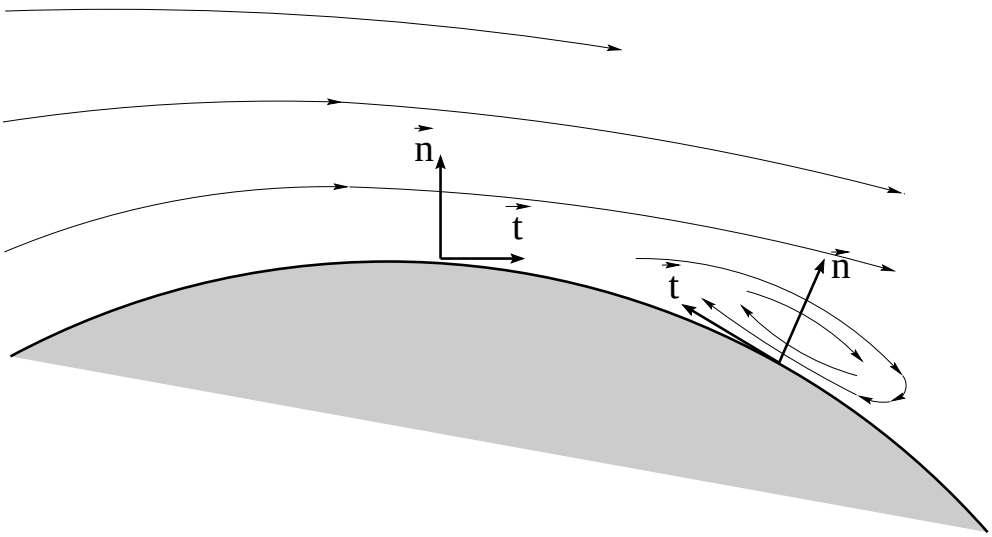

Figure 2.2: *Unit normal and tangential vector. The third base vector will be* $\vec{\tau} = \vec{t} \times \vec{n}$

$(\overline{uu})' = 1.098k$, $(\overline{vv})' = 0.247k$ and $(\overline{uv})' = -0.255k$, where $k = U_*^2/\sqrt{c_\mu}$. Note that, as a result of symmetry, $(\overline{vw})' = (\overline{wu})' = 0$. U_* is computed from the log law. A simple coordinate transformation will then produce the following Cartesian stresses at the node adjacent to the wall

$$
\begin{aligned}
\overline{uu} &= t_x{}^2(\overline{uu})' + n_x{}^2(\overline{vv})' + 2\,t_x\,n_x\,(\overline{uv})' \\
&\quad +(\overline{ww})'\,t_y{}^2 n_z{}^2 - 2\,(\overline{ww})'\,t_y\,n_z\,t_z\,n_y + (\overline{ww})'\,t_z{}^2 n_y{}^2 \\
\overline{vv} &= t_y{}^2(\overline{uu})' + n_y{}^2(\overline{vv})' + 2\,t_y\,n_y\,(\overline{uv})' \\
&\quad +(\overline{ww})'\,t_z{}^2 n_x{}^2 - 2\,(\overline{ww})'\,t_z\,n_x\,t_x\,n_z + (\overline{ww})'\,t_x{}^2 n_z{}^2 \\
\overline{ww} &= t_z{}^2(\overline{uu})' + n_z{}^2(\overline{vv})' + 2\,t_z\,n_z\,(\overline{uv})' \\
&\quad +(\overline{ww})'\,t_x{}^2 n_y{}^2 - 2\,(\overline{ww})'\,t_x\,n_y\,t_y\,n_x + (\overline{ww})'\,t_y{}^2 n_x{}^2 \\
\overline{uv} &= t_y\,t_x\,(\overline{uu})' + t_y\,n_x\,(\overline{uv})' + n_y\,t_x\,(\overline{uv})' + n_y\,n_x\,(\overline{vv})' \\
&\quad +(\overline{ww})'\,t_y\,n_z\,t_z\,n_x - (\overline{ww})'\,t_y\,n_z{}^2 t_x - (\overline{ww})'\,t_z{}^2 n_y\,n_x \\
&\quad +(\overline{ww})'\,t_z\,n_y\,t_x\,n_z \\
\overline{vw} &= t_z\,t_y\,(\overline{uu})' + t_z\,n_y\,(\overline{uv})' + n_z\,t_y\,(\overline{uv})' + n_z\,n_y\,(\overline{vv})' \\
&\quad +(\overline{ww})'\,t_z\,n_x\,t_x\,n_y - (\overline{ww})'\,t_z\,n_x{}^2 t_y - (\overline{ww})'\,t_x{}^2 n_z\,n_y \\
&\quad +(\overline{ww})'\,t_x\,n_z\,t_y\,n_x \\
\overline{wu} &= t_z\,t_x\,(\overline{uu})' + t_z\,n_x\,(\overline{uv})' + n_z\,t_x\,(\overline{uv})' + n_z\,n_x\,(\overline{vv})' \\
&\quad +(\overline{ww})'\,t_y\,n_z\,t_x\,n_y - (\overline{ww})'\,t_y{}^2 n_z\,n_x - (\overline{ww})'\,t_z\,n_y{}^2 t_x \\
&\quad +(\overline{ww})'\,t_z\,n_y\,t_y\,n_x
\end{aligned}
\tag{2.27}
$$

Note that this procedure will always give the proper sign for $\overline{uv}$ in a recirculating two-dimensional flow.

2.3.2 The Gibson and Launder wall reflection

The GL model is a modification of the IP model. It consists of the IP model terms and extra terms that correct the erroneous behaviour of the IP-model close to walls. The model is

$$\phi_{ij} = \phi_{ij,1} + \phi_{ij,2} + \phi_{ij}^{(w)} \tag{2.28}$$

$$\begin{aligned}\phi_{ij}^{(w)} = & \left(-c_1'\frac{\varepsilon}{k}\left(\overline{u_l u_m}\hat{n}_l\hat{n}_m\delta_{ij} - \frac{3}{2}\overline{u_i u_l}\hat{n}_l\hat{n}_j - \frac{3}{2}\overline{u_l u_j}\hat{n}_l\hat{n}_i\right)\right. \\ & \left. +c_2'\left(\phi_{lm,2}\hat{n}_l\hat{n}_m\delta_{ij} - \frac{3}{2}\phi_{il,2}\hat{n}_l\hat{n}_j - \frac{3}{2}\phi_{lj,2}\hat{n}_l\hat{n}_i\right)\right)\frac{k^{1.5}}{2.5\varepsilon y}\end{aligned} \tag{2.29}$$

where $\phi_{ij,1}$ and $\phi_{ij,2}$ are taken from the IP-model and the new constants are

$$c_1' = 0.5 \qquad c_2' = 0.3$$

$\hat{n}_i$ is the unit wall normal vector. If more than one wall normal exists, only the closest wall is incorporated, see figure 2.3.

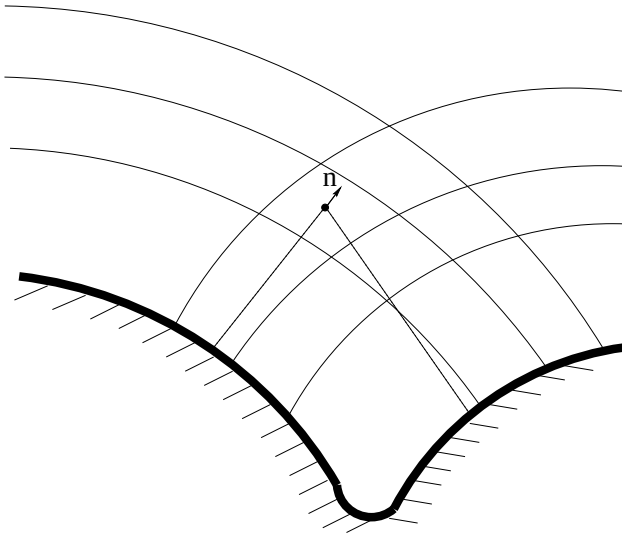

Figure 2.3: *Evaluation of the wall normal unit vector.*

The dissipation tensor, the dissipation rate equation and the wall boundary conditions are modeled as in the IP model described in Section 2.3.1.

2.3.3 A non-linear RSM. The SSG model

The model of Speziale, Sarkar and Gatski [33] is a fairly recent model that models the pressure strain interaction term by a non-linear relation of the anisotropy tensor, b_{ij}.

$$\begin{aligned}\phi_{ij} = & -\left(c_1\varepsilon + c_1^* P_k\right) b_{ij} + c_2\varepsilon\left(b_{ik}b_{kj} - \frac{1}{3}b_{kl}b_{kl}\delta_{ij}\right) \\ & +kS_{ij}\left(c_3 - c_3^*\sqrt{\mathrm{II}}\right) + c_4 k\left(b_{ik}S_{jk} + b_{jk}S_{ik} - \frac{2}{3}b_{kl}S_{kl}\delta_{ij}\right) \\ & +c_5 k\left(b_{ik}\Omega_{jk} + b_{jk}\Omega_{ik}\right)\end{aligned} \tag{2.30}$$

where

$$S_{ij} = \tfrac{1}{2}\left(\tfrac{\partial U_i}{\partial x_j} + \tfrac{\partial U_j}{\partial x_i}\right), \quad \Omega_{ij} = \tfrac{1}{2}\left(\tfrac{\partial U_i}{\partial x_j} - \tfrac{\partial U_j}{\partial x_i}\right)$$

$$b_{ij} = \frac{\overline{u_i u_j} - \frac{2}{3}k\delta_{ij}}{2k}, \qquad \mathbb{II} = b_{ij}b_{ji}$$

The SSG model seems to work fairly well without wall reflection terms, which is an important feature for the success of any model intended to be used on flows in or around advanced geometries including several wall normals within the domain. The constants are

$$c_1 = 3.4 \quad c_1^* = 1.8 \quad c_2 = 4.2$$
$$c_3 = 0.8 \quad c_3^* = 1.3 \quad c_4 = 1.25 \quad c_5 = 0.4$$

The SSG model is also a high Reynolds number model, and the dissipation tensor, the dissipation rate equation and the wall boundary conditions are modeled as in the IP model described in Section 2.3.1.

2.3.4 A low Reynolds RSM. The HL model

The low Reynolds number model proposed by Hanjalić and Launder [17] uses the linear pressure strain model proposed by Launder *et al.* [23],

$$\begin{aligned}\phi_{ij} = & \underbrace{-c_1\frac{\varepsilon}{k}\left(\overline{u_i u_j} - \frac{2}{3}\delta_{ij}k\right)}_{\phi_{ij,1}} \\ & \underbrace{-\frac{(c_2+8)}{11}\left(P_{ij} - \frac{2}{3}\delta_{ij}P_k\right) - \frac{60c_2-4}{55}S_{ij} - \frac{8c_2-2}{11}\left(\mathcal{D}_{ij} - \frac{2}{3}\delta_{ij}P_k\right)}_{\phi_{ij,2}} \\ & + \underbrace{\left(0.125\frac{\varepsilon}{k}\left(\overline{u_i u_j} - \frac{2}{3}k\delta_{ij}\right) + 0.015\left(P_{ij} - \mathcal{D}_{ij}\right)\right)\frac{k^{3/2}}{\varepsilon y}}_{\phi_{ij,w}}\end{aligned} \tag{2.31}$$

where y is the normal distance to the wall and

$$\mathcal{D}_{ij} = -\left(\overline{u_i u_k}\frac{\partial U_k}{\partial x_j} + \overline{u_j u_k}\frac{\partial U_k}{\partial x_i}\right)$$

The model constants c_1 and c_2 take the values 1.5 and 0.4, respectively. The dissipation tensor is modeled as

$$\varepsilon_{ij} = \frac{2}{3}\varepsilon\left((1-f_s)\delta_{ij} + \frac{\overline{u_i u_j}}{2k/3}f_s\right) \tag{2.32}$$

where the damping function is chosen as $f_s = (1 + R_T/10)^{-1}$, see [17]. Modifications are also introduced in the dissipation equation, which in this low Reynolds number proposal has the form

$$\begin{aligned}\frac{D\varepsilon}{Dt} = & c_{\varepsilon 1}\frac{\varepsilon}{k}P_k - c_{\varepsilon 2}f_2\frac{\varepsilon\tilde{\varepsilon}}{k} + c_{\varepsilon 3}\nu\frac{k}{\varepsilon}\overline{u_j u_k}\left(\frac{\partial^2 U_i}{\partial x_j \partial x_l}\right)\left(\frac{\partial^2 U_i}{\partial x_k \partial x_l}\right) \\ & + \frac{\partial}{\partial x_k}\left(\nu\frac{\partial \varepsilon}{\partial x_k} + \frac{c_s}{\sigma_\varepsilon}\frac{k}{\varepsilon}\overline{u_k u_l}\frac{\partial \varepsilon}{\partial x_l}\right)\end{aligned} \tag{2.33}$$

where

$$c_{\varepsilon 1} = 1.275 \quad c_{\varepsilon 2} = 1.8 \quad c_{\varepsilon 3} = 2.0$$

$$f_2 = 1 - 2/9 \exp\left(-(R_T/6)^2\right)$$

$$\tilde{\varepsilon} = \varepsilon - 2\nu \left(\frac{\partial \sqrt{k}}{\partial x_l}\right)^2 \qquad R_T = \frac{k^2}{\nu \varepsilon}$$

Wall boundary conditions

Since this model is a low Reynolds number model, it integrates the boundary layer to the wall. Thus the no-slip boundary condition is valid. A homogeneous Dirichlet boundary condition is imposed on velocities and stresses. The dissipation rate is set to $2\nu \left(\frac{\partial \sqrt{k}}{\partial x_l}\right)^2$ at the wall.

2.3.5 A cubic realizable RSM. The LLI model

This model is one of few realizable pressure strain models in the literature. It is a cubic proposal from UMIST that, in the form proposed by Launder and Li [22], seems to work quite well without wall reflection terms. The pressure strain term reads:

$$\phi_{ij} = \phi_{ij,1} + \phi_{ij,2} \tag{2.34}$$

where

$$\phi_{ij,1} = \left(-c_1 \varepsilon \left(a_{ij} + c_1'(a_{ik}a_{jk} - \frac{1}{3}A_2\delta_{ij})\right) - \varepsilon a_{ij}\right)(1 - f_\varepsilon) \tag{2.35}$$

$$\begin{aligned}
\phi_{ij,2} = & -0.6(P_{ij} - \frac{2}{3}\delta_{ij}P_k) + 0.6a_{ij}P_k \\
& -0.2\left(\frac{\overline{u_k u_j}\,\overline{u_l u_i}}{k}\left(\frac{\partial U_k}{\partial x_l} + \frac{\partial U_l}{\partial x_k}\right) - \frac{\overline{u_l u_k}}{k}\left(\overline{u_i u_k}\frac{\partial U_j}{\partial x_l} + \overline{u_j u_k}\frac{\partial U_i}{\partial x_l}\right)\right) \\
& -c_2\left(A_2(P_{ij} - \mathcal{D}_{ij}) + 3a_{mi}a_{nj}(P_{mn} - \mathcal{D}_{mn})\right) \\
& +c_2'\left(\left(\frac{7}{15} - \frac{A_2}{4}\right)(P_{ij} - \frac{2}{3}\delta_{ij}P_k)\right. \\
& +0.2\left(a_{ij} - \frac{1}{2}(a_{ik}a_{kj} - \frac{1}{3}\delta_{ij}A_2)\right)P_k - 0.05a_{ij}a_{lk}P_{kl} \\
& +0.1\left(\left(\frac{\overline{u_i u_m}}{k}P_{mj} + \frac{\overline{u_j u_m}}{k}P_{mi}\right) - \frac{2}{3}\delta_{ij}\frac{\overline{u_l u_m}}{k}P_{ml}\right) \\
& +0.1\left(\frac{\overline{u_l u_i}\,\overline{u_k u_j}}{k^2} - \frac{1}{3}\delta_{ij}\frac{\overline{u_l u_m}\,\overline{u_k u_m}}{k^2}\right)\left(6\mathcal{D}_{lk} + 13k\left(\frac{\partial U_l}{\partial x_k} + \frac{\partial U_k}{\partial x_l}\right)\right) \\
& \left.+0.2\,\frac{\overline{u_l u_i}\,\overline{u_k u_j}}{k^2}(\mathcal{D}_{lk} - P_{lk})\right)
\end{aligned} \tag{2.36}$$

where

$$a_{ij} = \frac{\overline{u_i u_j} - \frac{2}{3}k\delta_{ij}}{k} \qquad A_2 = a_{ij}a_{ij} \qquad c_1 = 3.1\sqrt{A_2 A}$$
$$c_1' = 1.2 \qquad A_3 = a_{ik}a_{kj}a_{ji} \qquad A = 1 - 9/8\,(A_2 - A_3)$$
$$c_2 = 0.55 \qquad c_2' = 0.6 \qquad f_\varepsilon = 0$$

The LLI model is a high Reynolds number model, and the dissipation tensor, the dissipation rate equation and the wall boundary conditions are modeled according to the IP model described in section 2.3.1.

2.3.6 A cubic and realizable low Reynolds number RSM. A proposed model

This is a mix of two other models described above, and thus the pressure strain interaction term from the LLI model is combined with the dissipation tensor from the HL model. Some modifications must be made to maintain realizability. The slow pressure strain term must use a damping function, f_ε, equal to that used in the dissipation tensor, since one of the realizability demands is that the sum of the dissipation term, ε_{ij}, and the slow pressure strain term, $\phi_{ij,1}$, should go to zero if the corresponding Reynolds stress goes to zero. This requirement will not be fulfilled unless the damping function is also used on the slow pressure strain term. The damping function is chosen as $f_\varepsilon = \sqrt{A}$ and is used in equations (2.32) and (2.35). Furthermore, the constants in the rapid part of the pressure strain term, equation (2.36), is modified, as suggested by Craft and Launder [11], to

$$c_2 = \min(0.55, (AA_2)^{3/2}) \quad c_2' = \min(0.6, (AA_2)^{3/2})$$

Chapter 3

Simulation of the flow around an axisymmetric body

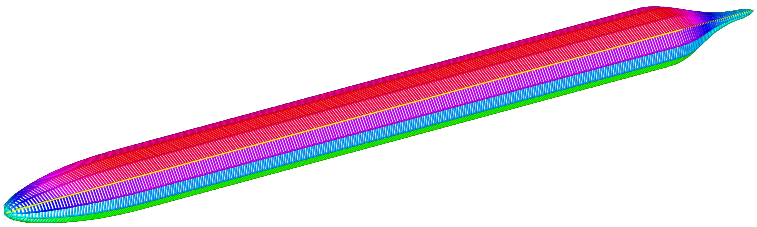

An axisymmetric body with a smooth rear end was chosen as a first test case. Experimental data exists, Huang *et al.* [18], for two Reynolds numbers, namely: $Re_L = 5.9 \cdot 10^6$ and $Re_L = 8.8 \cdot 10^6$. The test case was computed before any of the source code was available, and three different turbulence models were used. Since there is more experimental data available at $Re_L = 5.9 \cdot 10^6$, the computations were focused on this Reynolds number.

3.1 Turbulence models

As stated above, three turbulence models were used in the computations, the standard k-ε model using wall functions, see Section 2.2.1, together with a low Reynolds number proposal by Launder and Sharma [24], see Section 2.2.2. A RSM was also used, which is the IP model described in Section 2.3.1.

3.2 The mesh

The grids used in the computations are a one-block structured mesh consisting of cells for the two high Reynolds number models and cells for the low Reynolds number model, see figure 3.1. The centers of the innermost cells were located at distances of $y^+ = 30$ and $y^+ = 0.1$, respectively.

3.3 Convection scheme

The higher order upwind scheme, HUW see [3], is used when discretizing the convection terms in the momentum equations. The first-order accurate hydrid scheme

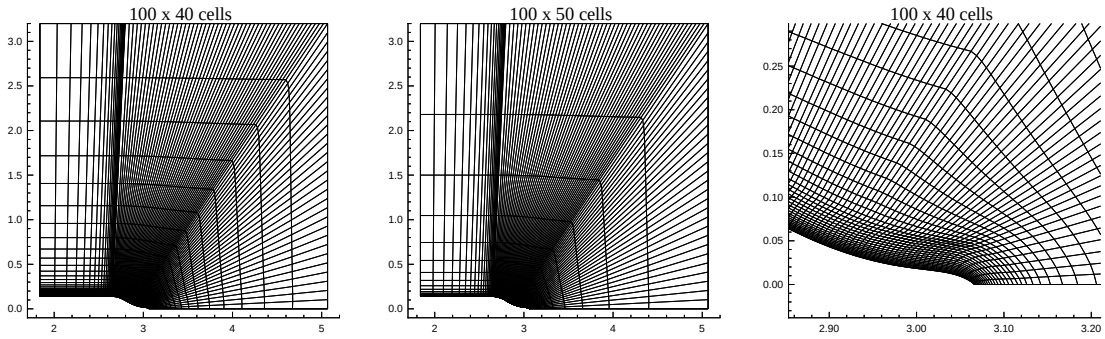

Figure 3.1: *A* **100***x***40** *mesh made for wall functions and a* **100***x***50** *mesh made for use with the low Re k-ε model. To the right an enlargement of the region of the rear end is shown.*

is used for ditto in all turbulence equations.

3.4 Boundary conditions

Inlet conditions were obtained using the results of a previous computation of a circular channel. The reasoning was as follows. Homogeneous profiles were set to U according to the Reynolds number in the experiments. The V velocity was of course set to zero, and turbulent quantities were set to low positive values, except for the $\overline{uv}$-stress, which was set to zero. The axisymmetric channel flow was computed, from which a profile was to be selected. The inlet was chosen to be at $x/L = 0.6$, where only the skin friction coefficient was available from measurements. Thus the inlet profiles of all variables could be taken where the channel flow reached this skin friction coefficient.

Outlet conditions were set as homogeneous Neuman conditions for all variables.

3.5 Results

A small separation bubble is present in the experiments at $x/L = 0.918$ but no separation occured in the computations. one could use The sign of the friction coefficient, c_f, can be used as a criterion of separation, and as can be seen in figure 3.2, the RSM (IP model) is closer to separation than the k-ε model. The pressure distributions along the surface of the body are shown in figure 3.3, and computations agree well for all models except at what should be the separated region, where the IP model proves to be more accurate than the standard k-ε model. The low Reynolds number k-ε model did not give results since no convergence was reached. This is due to the fact that, during iterations, the solution oscillates between two steady state solutions, separated and not separated. In the computations using the low Reynolds number k-ε model and $Re_L = 8.8 \cdot 10^6$, a stable solution is reached and separation occurs at $x/L = 0.912$, see figure 3.4. The high Reynolds number models did not separate for this Reynolds number.

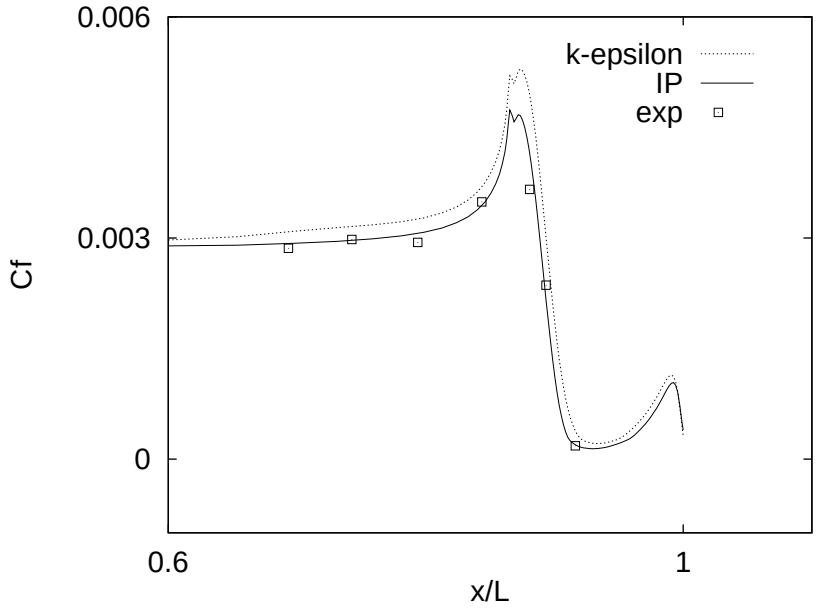

Figure 3.2: c_f *at* $Re_L = 5.9 \cdot 10^6$.

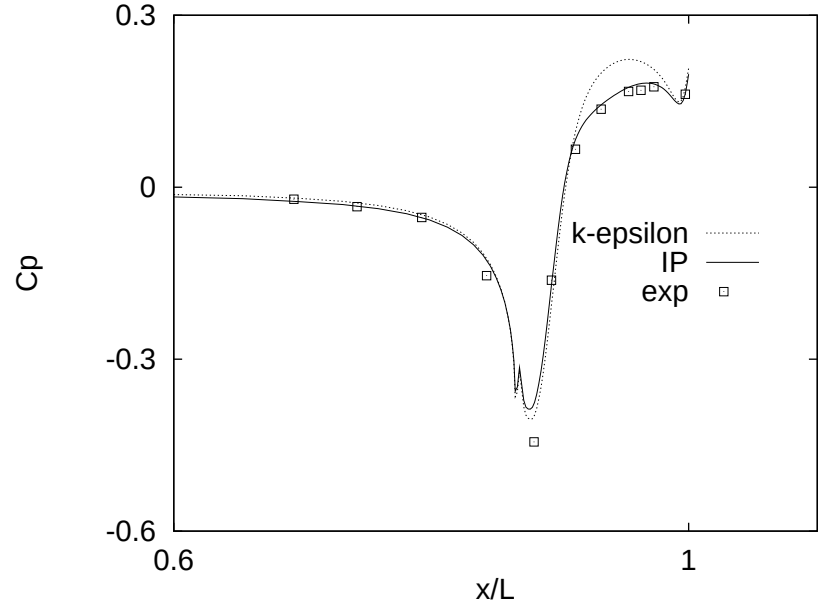

Figure 3.3: c_p *at* $Re_L = 5.9 \cdot 10^6$.

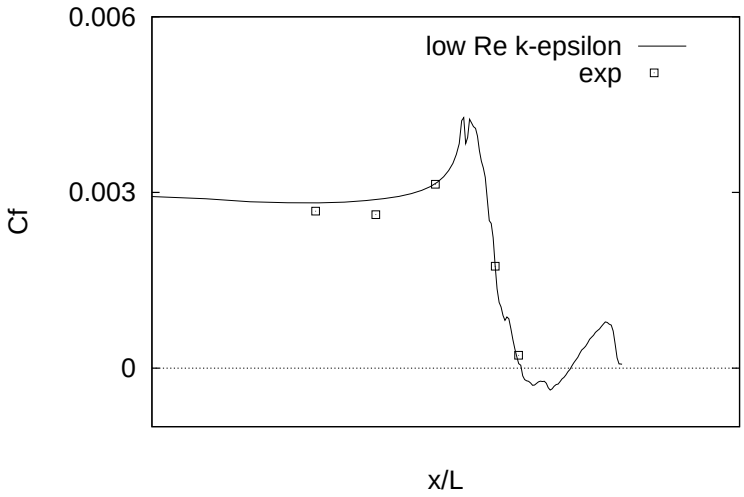

Figure 3.4: c_f *at* $Re_L = 8.8 \cdot 10^6$.

3.6 Conclusions

It can be concluded that RSM works better than the k-ε model and that wall functions do not work very well when a separation should occur. Approaching the separation point, wall functions are no longer valid and thus give rise to discrepancies. The low Re k-ε model seems to work even better than the RSM. The flow separates at $Re_L = 8.8 \cdot 10^6$ with this model, which does not occur when the other models are used. However, this comparison is not very relevant since the RSM was wall function-based. A more interesting comparison would be to test this low Reynolds number k-ε model versus some low Reynolds number RSM.

Wall reflection terms in the pressure-strain term are excluded in CFDS-FLOW3D. This is because it is almost impossible to implement these terms in a general way. This fact is also a source of discrepancies in wall-bounded flows and will be investigated below.

Chapter 4

Channel Flow

A two-dimensional channel flow was computed chiefly for debugging purposes as a simple and CPU-effective test case. Experiments by Laufer [21] are available. The Reynolds number based on the maximum velocity and half the height of the channel is $Re_{h/2} = 30\,800$.

4.1 Turbulence models

Reynolds stress models were used and the models are, the IP model, the GL model, the SSG model, the LLI model and the Present model. All models are thoroughly described in section 2.3.

4.2 Convection scheme

The higher order upwind scheme, HUW see [3], is used in the momentum equations, and the hydrid scheme is used in all turbulence equations.

4.3 Results 2D channel flow

The IP model gives an erroneous normal stress distribution, which can be seen directly from the pressure strain interaction term, equation (2.24). The production terms for the $\overline{vv}$ stress and the $\overline{ww}$ stress are zero, and thus equations (2.6) are identical for both stresses and thus

$$\overline{vv} = \overline{ww}$$

using this model. The $\overline{vv}$ stress is overpredicted close to the wall and will give rise to the overpredicted $\overline{uv}$ stress, see figure 4.1.

Wall reflection terms will solve this problem as in the GL model, see figures 4.2-4.4. Since wall reflection terms include wall normal distances and wall normal unit vectors, these are not very useful in codes of any generality. Models that mimic the presence of a wall without wall distances are instead preferred, such as the SSG model. This captures the stress distribution in essence, see figures 4.2-4.4. The LLI model works even better and shows better accuracy on the 2D channel flow than any other model. A truncated form of this model was also tested with constants

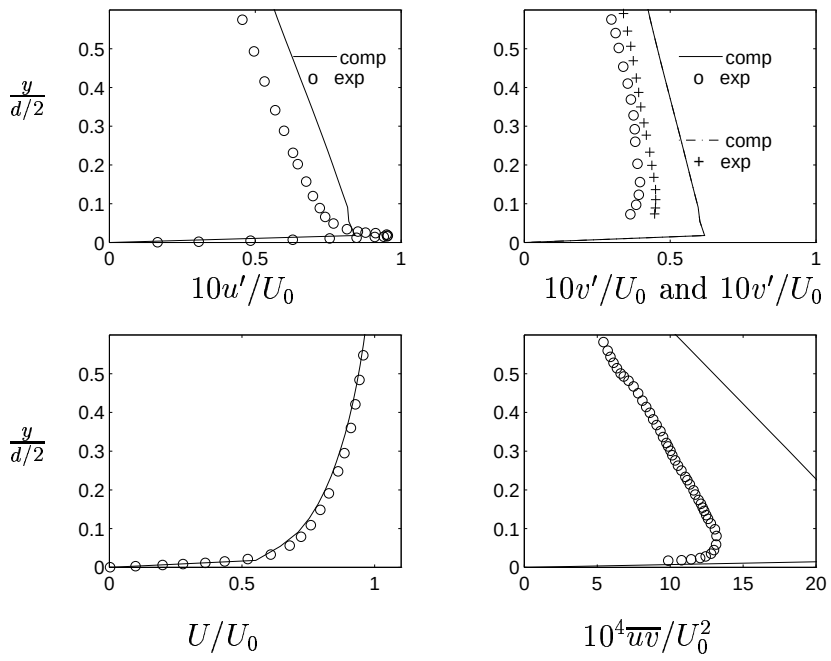

Figure 4.1: *2D channel flow using the IP model.*

according to Craft [10], that is $c_2 = 0.6$ and $c_2' = 0$ in equation 2.36. This model, called the CS model, gave an accuracy comparable to that obtained using the SSG model, see figures 4.2-4.4.

No significant benefits are gained by using a low Reynolds number model, as wall functions are designed for and work very well on this fully developed boundary layer. The channel flow was used for the constants in the Present model, and the results from that model are shown in figures 4.5 and 4.6.

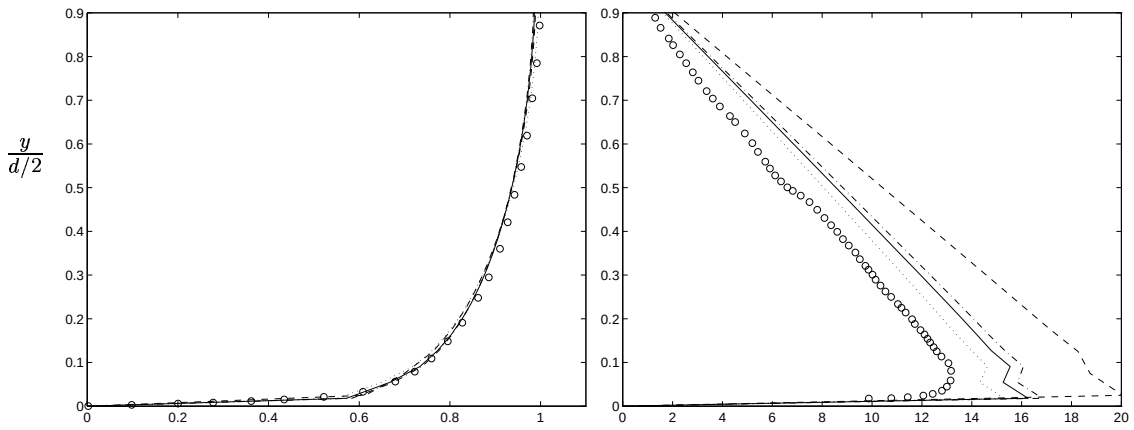

Figure 4.2: *U velocity and $\overline{uv}$ profiles from the 2D channel flow using RSMs.*

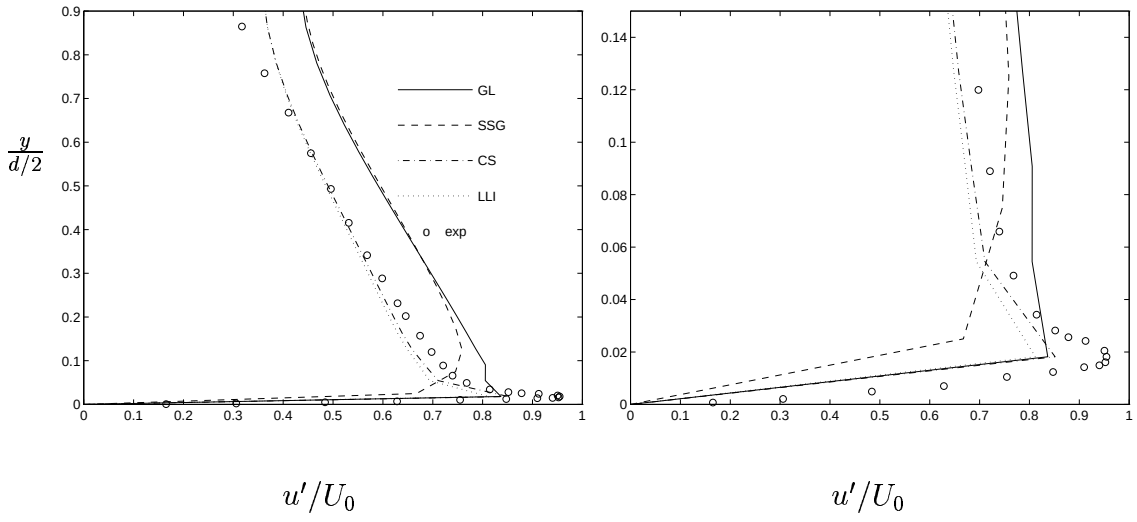

Figure 4.3: *u' profiles from the 2D channel flow using RSMs*

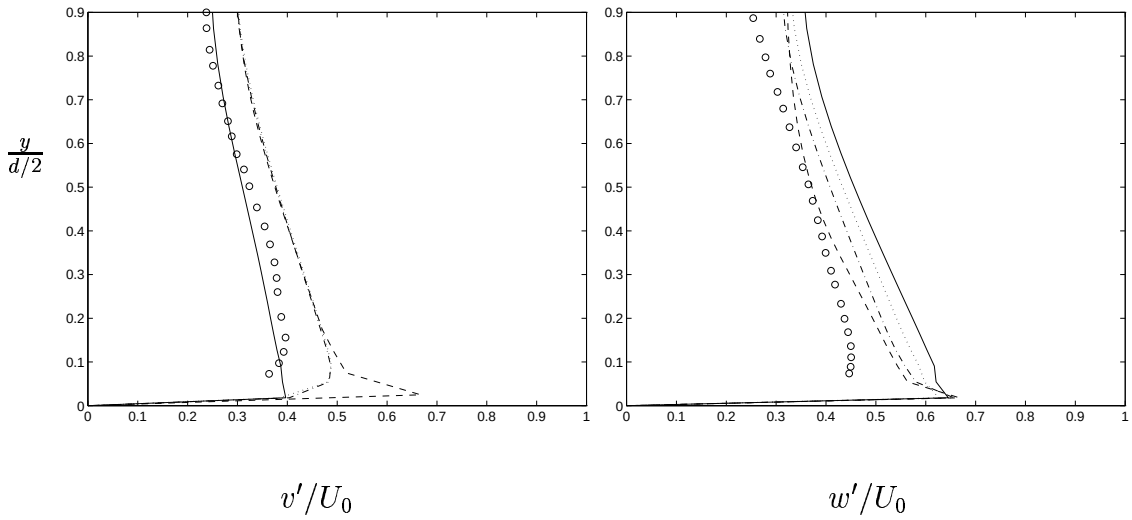

Figure 4.4: *v' and w' profiles from the 2D channel flow using RSMs. Legend according to Figure 4.3*

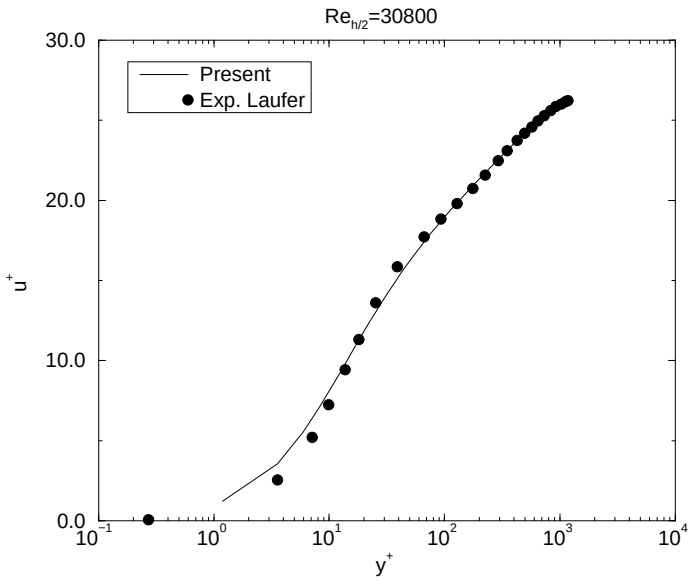

Figure 4.5: *2D channel flow using the Present model. Velocity profile.*

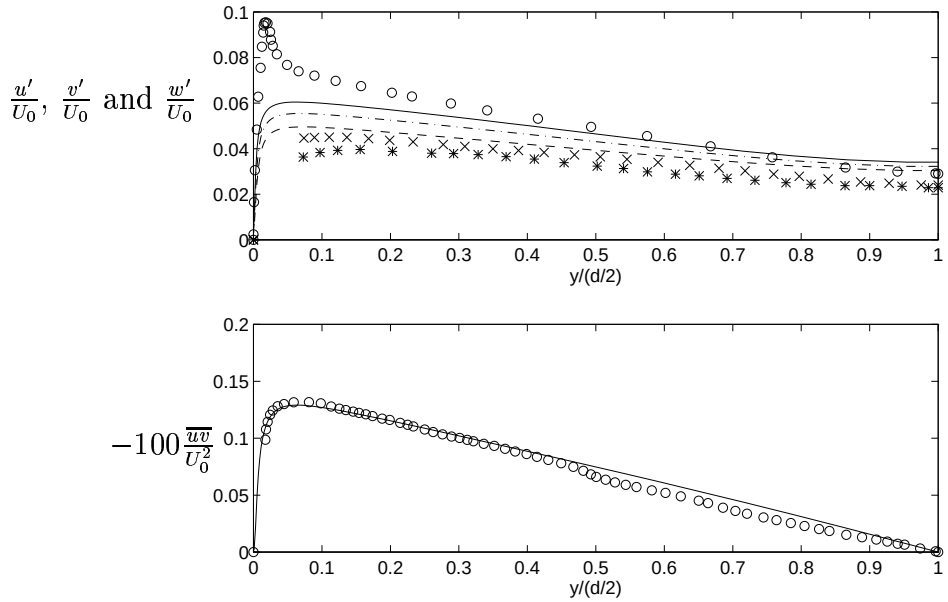

Figure 4.6: *2D channel flow using the Present model. Stress distribution. u' is plotted by the solid line and the "o" symbol, v' by the dashed line and the "*" symbol and w' by the dashed dotted line and the "x" symbol.*

Chapter 5

The flow over a backward-facing step

The flow over a backward-facing step was computed using a low Reynolds number RSM. There are DNS data by Le & Moin [26].

5.1 Turbulence models

Reynolds stress models were used modelling the turbulence on the backward-facing step. The models used are:

- The IP model described in section 2.3.1.
- The GL model described in section 2.3.2.
- The LLI model described in section 2.3.5.
- The Present model described in section 2.3.6.

5.2 Convection scheme

The higher order upwind scheme, HUW see [3], is used in the momentum equations, and the hydrid scheme is used in all turbulence equations.

5.3 Flow description

The computational domain is shown in figure 5.1, and the Reynolds number based on the step height and free stream velocity is $Re_h = 5\,100$. Inlet profiles are taken from DNS data, and the inlet is located 10 step heights upstream of the step. The expansion ratio is 1.2, and the outlet is placed sufficiently far downstream for a homogeneous Neumann boundary condition, that is 30 step heights. The meshes used consisted of two blocks. The number of cells are:

- 10 524 cells for the low Reynolds number mesh.
- 3 300 cells for the high Reynolds number mesh.

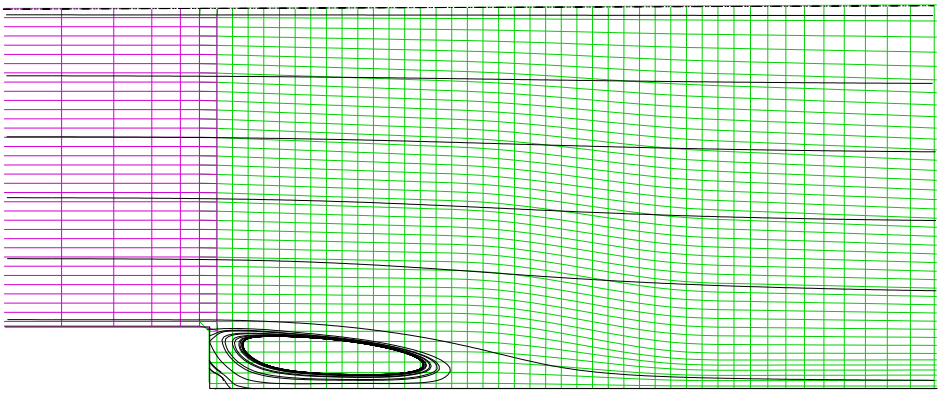

Figure 5.1: *The backward-facing step flow.*

5.4 Results

All high Reynolds number models reattach too rapidly, and the k-ε model reattached more rapidly than any of the RSMs, see the streamlines in figure 5.2. The present model reattached somewhat too late, see figure 5.3, because of an underprediction of the shear stress, $\overline{uv}$, in the shear region, see figure 5.4.

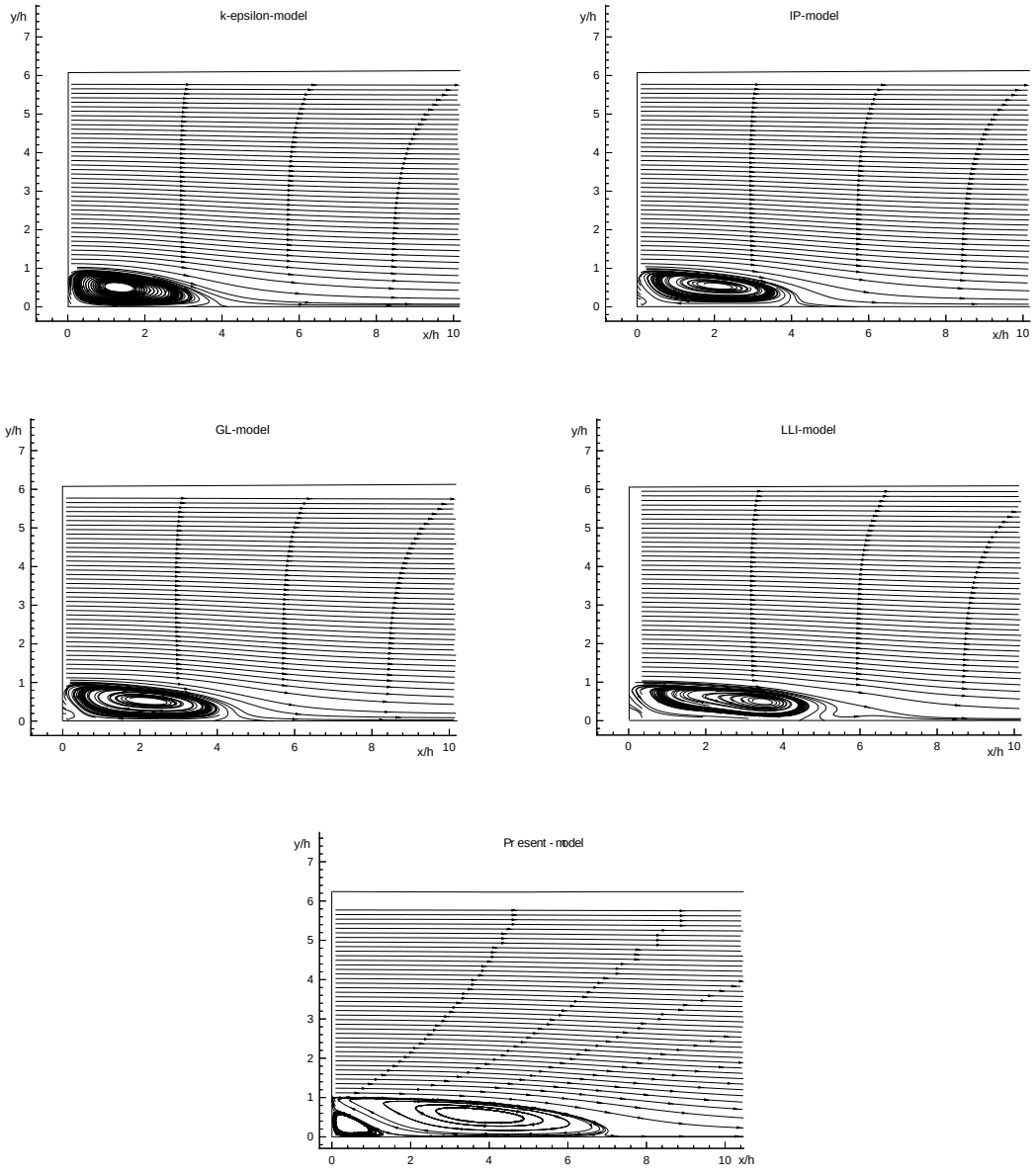

Figure 5.2: *Streamlines for the backward-facing step.*

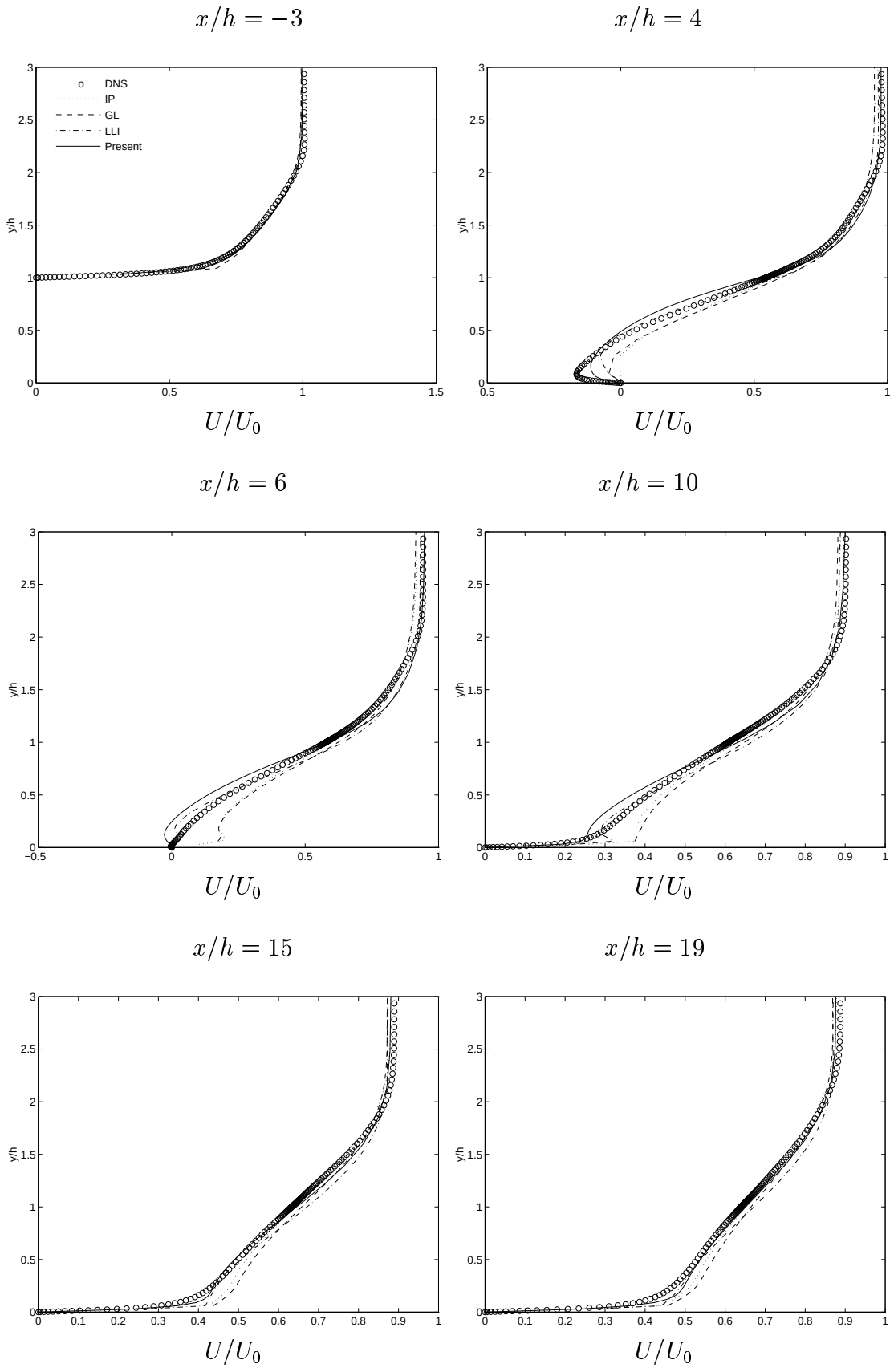

Figure 5.3: *The backward-facing step flow. U-velocity profiles at different x-locations.*

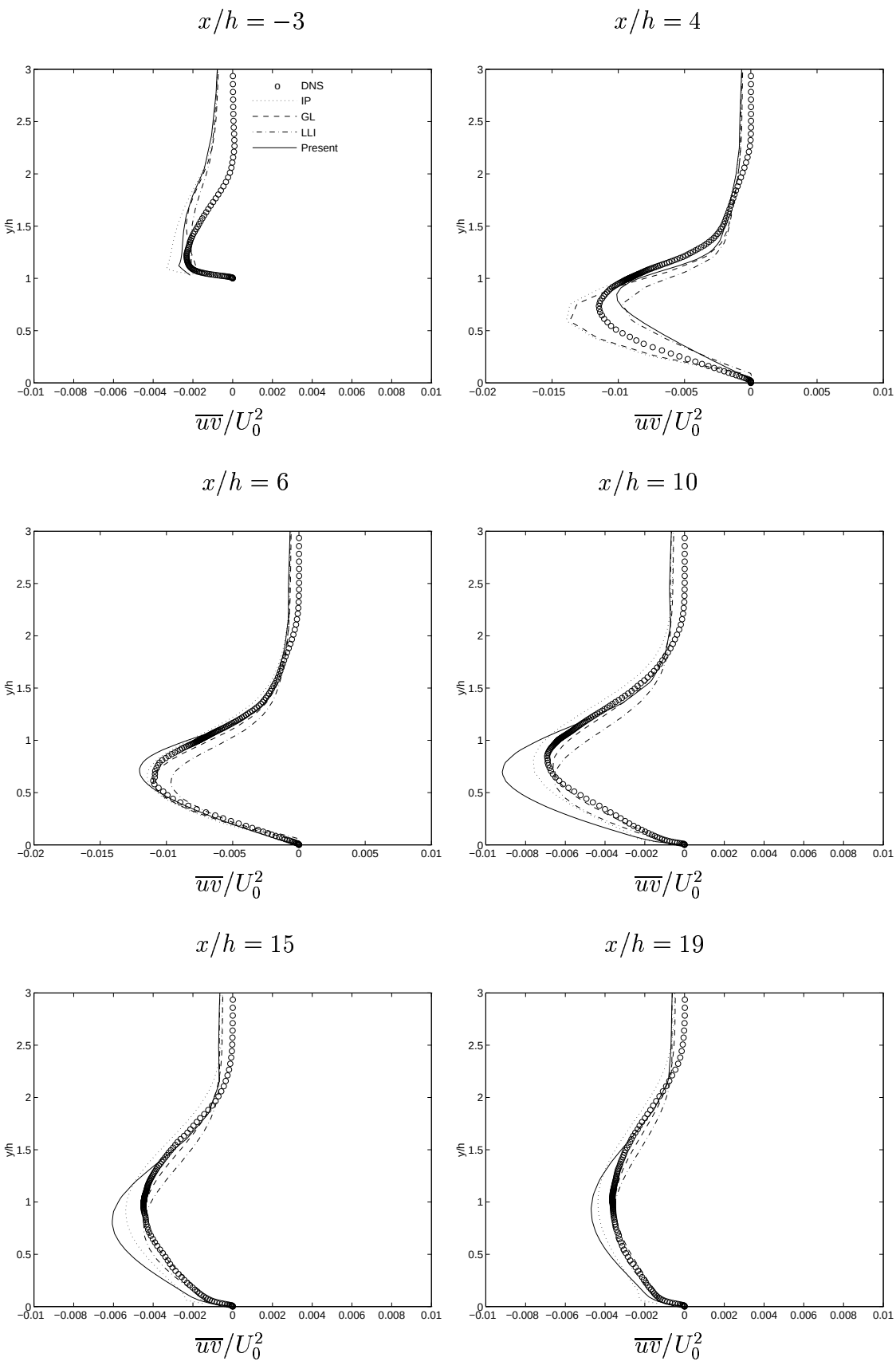

Figure 5.4: *The backward-facing step flow. $\overline{uv}$-profiles at different x-locations.*

Chapter 6

2D hill flows

The next test case chosen is the flow over a 2D hill, see figure 6.1, which is a test case in the ERCOFTAC/IAHR *Workshop on Databases and Testing of Calculation Methods for Turbulent Flows*, Karlsruhe 1994, [1], where these results were presented. This test case has been measured by Almeida *et al.* [5], and an extensive number of experimental data is available that includes turbulent quantities.

6.1 Flow description

The domain is shown in figure 6.1, and the geometrical parameters are

- Channel height, $H = 170$ mm
- Hill height, $h = 28$ mm

The top of the hill should be located 100 mm after the inlet and the outlet should be at a sufficient distance downstream. Furthermore, flow parameters are (water),

- Density, $\rho = 1000$ kg/m^3
- Kinematic viscosity, $\nu = 1 \cdot 10^{-6}$ m^2/s
- Mean centerline velocity at the inlet, $U_0 = 2.147$ m/s

This gives a Reynolds number of

$$Re_h = \frac{U_0 h}{\nu} = 60\,000$$

6.2 The mesh

The grids used were created using the ICEM-CFD mesh generator. The mesh sizes for different near-wall treatments are

- Wall function models: **122 x 50**, see figure 6.2
- Low Reynolds number models: **128 x 100**, see figure 6.3

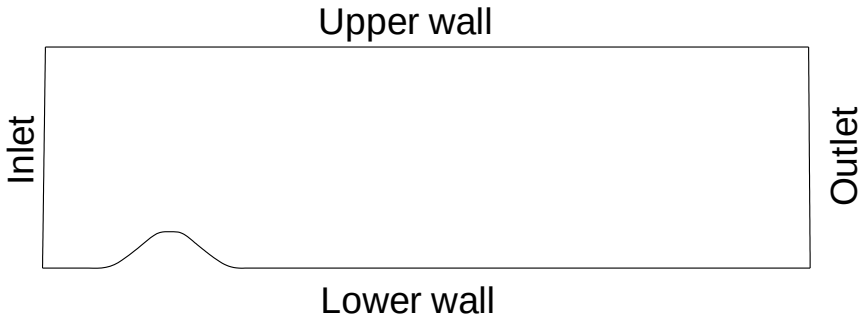

Figure 6.1: *Domain for 2D hill flow.*

6.3 Turbulence models

6.3.1 Two-equation models

The standard k-ε model described in Section 2.2.1 was used together with the low Reynolds number formulation of the model described in Section 2.2.2.

6.3.2 Reynolds Stress Models

The differential stress model is described in Section 2.3. Three high Reynolds number models were used and these are the IP model described in Section 2.3.1, the GL model described in Section 2.3.2 and the nonlinear SSG model described in Section 2.3.3.

A low Reynolds number RSM was also used, the HL model described in Section 2.3.4.

6.4 Convection schemes

The QUICK scheme is used for mean velocities and the hybrid scheme is used for k, ε and the Reynolds stresses in the differential stress models.

6.5 Results, 2D Hill Flow

The location of the separation point is estimated to be about $x_s = 0.012$ m after the hill top in the experiments, see [5]. Furthermore, the reattachment point is located at about 0.135 m beyond the top of the hill, which is $x/h = 4.82$.

This test case even increased the necessity for better near-wall models discussed in section 3.6. Wall function-based models completely fail in capturing the separation point and the separation is far too late. Thus the separated region becomes too small, see figure 6.4.

On the other hand, a more advanced pressure strain interaction term, e.g. the SSG model, see figure 6.5, shows that an improvement can be made by simply using

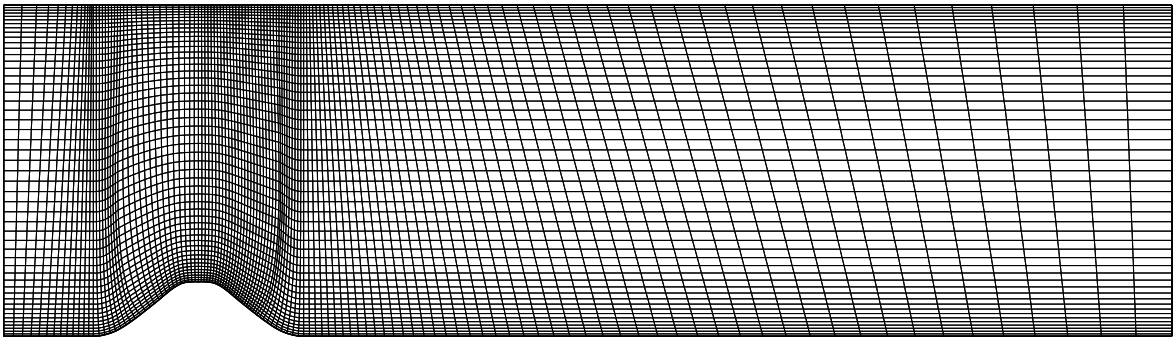

Figure 6.2: *Grid with 122x50 cells for 2D hill flow.*

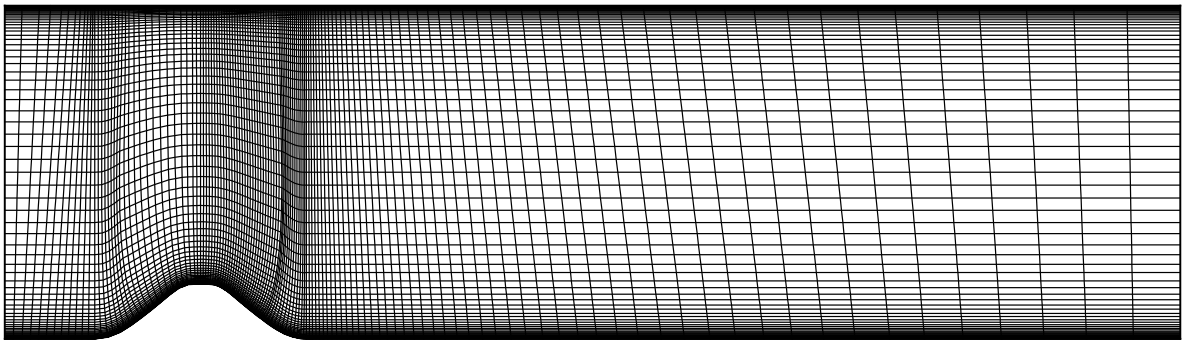

Figure 6.3: *Grid with 128x100 cells for 2D hill flow.*

a better turbulence model. However the separated region is still too small. The low Reynolds number k-ε model shows better agreement with experiments, in spite of the fact that the separation area is overpredicted in the first part of the bubble. The bubble recovers quickly and the reattachment point is accurately predicted. This means that the height of the separation region is overpredicted at the same time that its length is quite well predicted, see figure 6.6. The separation occurs at about $x = 0.010$ m, which is too early. The HL model proves to give the best agreement with experiments in predicting the separation point at $x = 0.015$ m, see figure 6.6. Thus, this model predicts the bubble height correctly and then recovers too quickly, rendering a separation bubble that is too short. The reattachment is therefore somewhat early; see figures 6.9 and 6.11 for a comparison of the mean flow with experiments. Furthermore, all high Reynolds number models tested show large discrepancies for the turbulent quantities in the separated region. This is of course due to the fact that the error that occurs when the location of the separation point is predicted becomes significant downstream. This error is then convected further

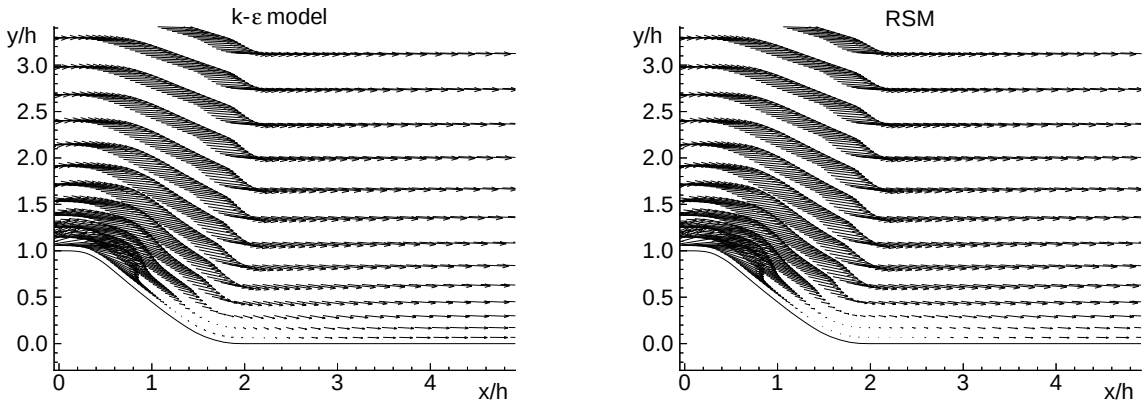

Figure 6.4: *Velocity vectors showing the separated region using the k-ε model and the GL model, respectively.*

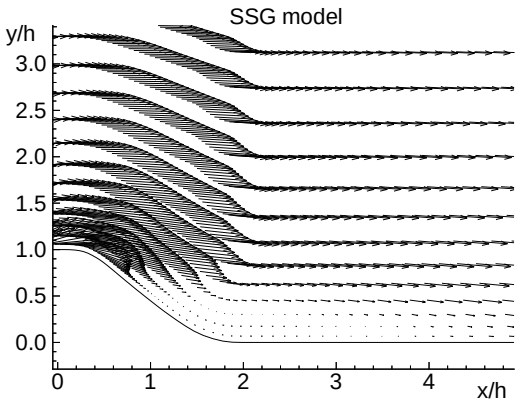

Figure 6.5: *Velocity vectors showing the separated region using the SSG model.*

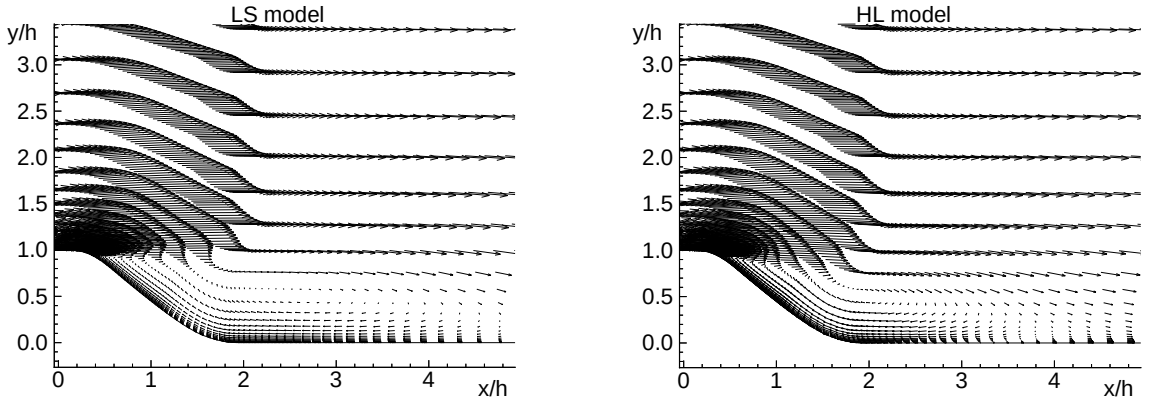

Figure 6.6: *Velocity vectors showing the separated region using the LS-model and the HL-model respectively.*

downstream, see figures 6.12, 6.13 and 6.14. The low Reynolds number models are much more accurate in this region. However, the LS model overpredicts the turbulent kinetic energy at the top of the hill. This is also true for the standard k-ε model, see figure 6.12. The reason for this is that the acceleration of the flow over the top or the blockage of the flow is known to create problems, causing too high a production of kinetic energy when k-ε models are used. RSMs such as the HL model do account for this phenomenon since the production terms in the stress equations are exact. Figure 6.12 also shows that there is better agreement with experiments with the HL model than the LS model in the first part of the separated region, whereas the LS model is more accurate in the rear part and in the far wake. This is natural since the flow attached too early using the HL model and downstream discrepancies thus occur as a consequence. Shear stress profiles are shown in figure 6.14 for the RSMs and indicate reasonably good agreement with experiments except for the latter part of the separated region as discussed above.

6.5.1 Curvature effects

It is interesting to see how the curvature of the flow affects turbulence in the models. Curvature can be measured by the curvature radius R_c

$$\frac{1}{R_c} = \left. \frac{d^2y/dx^2}{\left(1 + (dy/dx)^2\right)^{3/2}} \right|_{\psi=\text{const}}$$

high curvature radius $\Longleftrightarrow$ low curvature

With $dy/dx|_{\psi=\text{const}} = V/U$, this equation becomes

$$\frac{1}{R_c} = \frac{UV\left(\frac{\partial V}{\partial y} - \frac{\partial U}{\partial x}\right) + U^2\frac{\partial V}{\partial x} - V^2\frac{\partial U}{\partial y}}{\left(U^2 + V^2\right)^{3/2}} \tag{6.1}$$

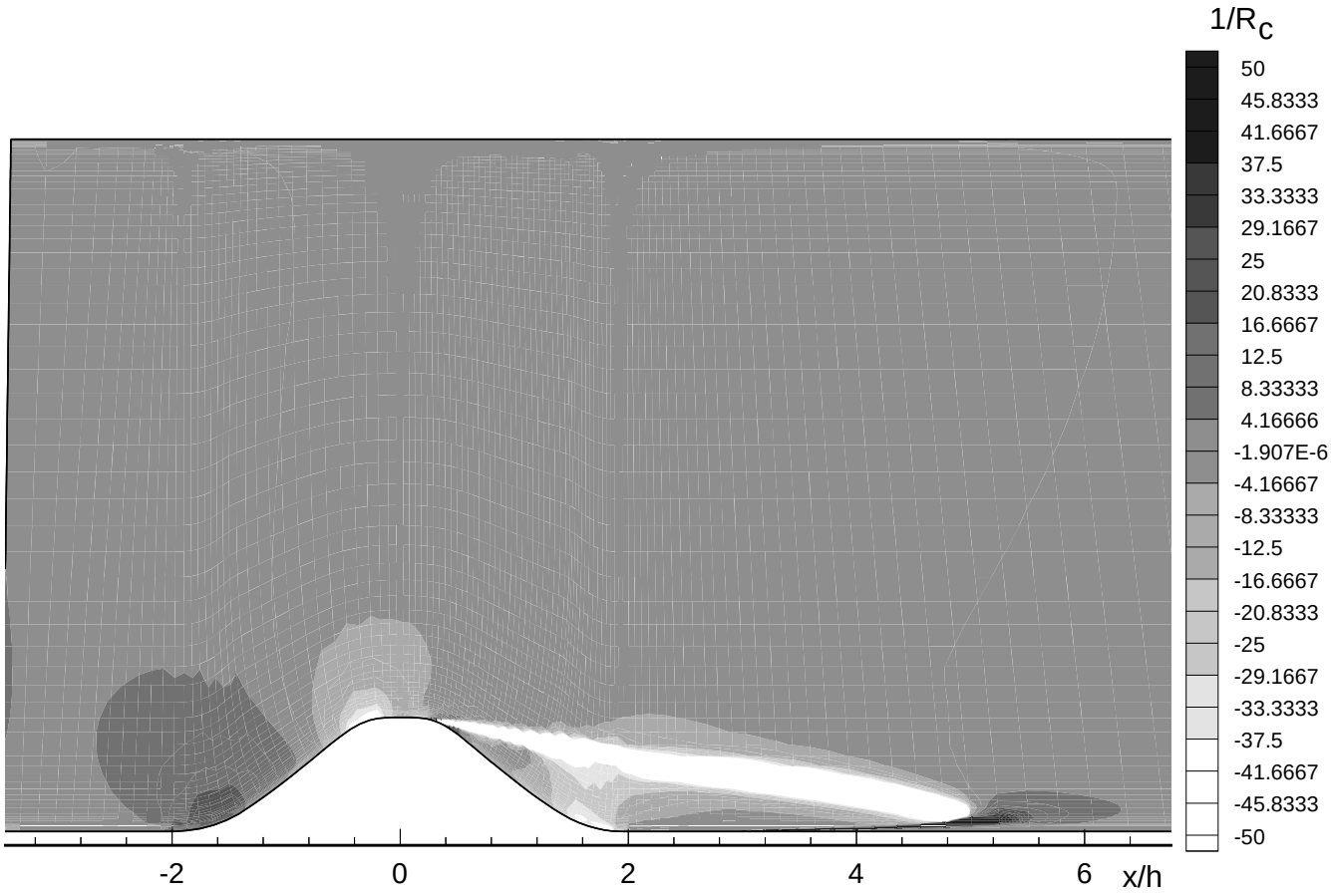

Figure 6.7: *Streamline curvature isocontours using the HL model.*

This quantity can graphically be visualized as in figure 6.7, where the peaks have been cut off at $1/R_c = \pm 50 m^{-1}$ in order to make changes visible. This cut-off value is two orders lower in magnitude than the highest and lowest peaks. Budgets of the shear stress equation at the location marked in figure 6.7 show rapid response to curvature changes. This is natural, but the question is whether the response is accurate. The production term is of course correct since it is exact. It is thus interesting to see how the modelled terms respond to a large streamline curvature change, see figure 6.8.

Streamline curvature effects are important, and present models do not fully describe how these affect turbulence. Proposals have been made for curvature corrections, see [9] and [29]. For a discussion of curvature effects see Davidson [14] and [13].

6.6 Conclusions, 2D Hill Flow

The first conclusion that can be drawn from the discussion above is that it is hazardous to use wall functions are in separated flows. It seems as though it is necessary

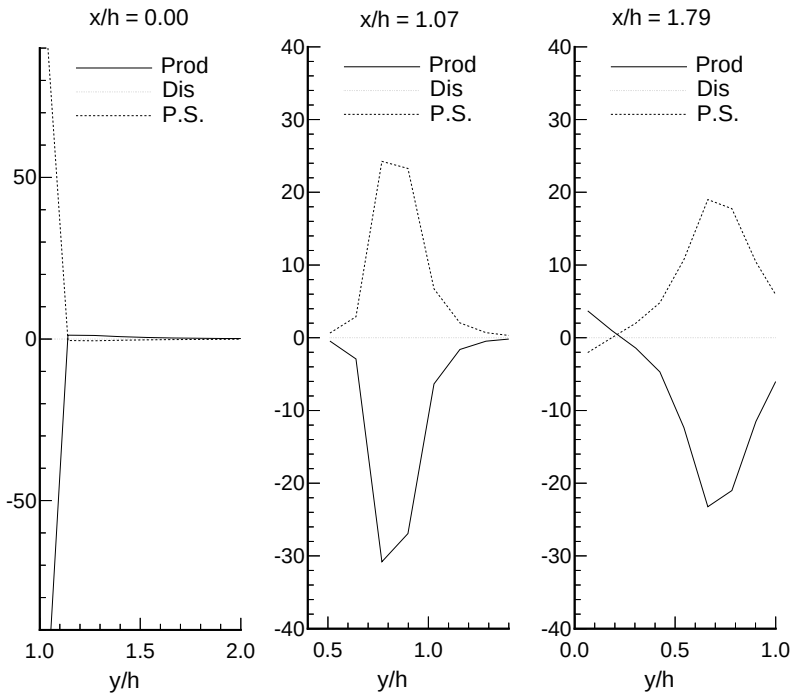

Figure 6.8: *Parts of $\overline{uv}$ budget at three x-locations using the HL-model. P.S. denotes the pressure strain interaction term.*

to resolve the boundary layer, including the viscous sublayer. While this is of course costly, it seems unevitable in advanced flows that include separation. It should be noted that results were presented by other researchers at the ERCOFTAC Workshop [1] where the standard k-ε model with wall functions gave impressive results. One reason may be a different approach for wall functions. Different grids, boundary conditions and convection schemes might also give rise to distinctions between solutions. There are two-layer proposals in the literature that might solve at least part of the problem with wall functions. However, most of these proposals require as fine a resolution as is necessary for low Reynolds number models.

Some improvements may also be made by using a more advanced pressure-strain interaction model, e.g. the SSG model. This model gave the best results among the tested high Reynolds number models. Another benefit gained from this model is that it does not seem to need wall compensation terms, which are difficult to implement in a general manner.

The low Reynolds number models proved to be much more accurate for this test case. The HL model predicts the location of the separation point more accurately than the LS model. Stability problems were present with both models although they were easily solved in the LS model adjusting underrelaxation factors. The HL model was extremely sensitive and unstable, and both the stresses and the rate of dissipation ε had to be heavily underrelaxated during the iteration process, which in turn leads to many iterations and long computational times. It would not be surprising for these convergence problems to even increase when problems in 3D are

computed. This is of course a major drawback in the HL model, since one of the basic demands of industry in using CFD is robustness and cost-effective codes.

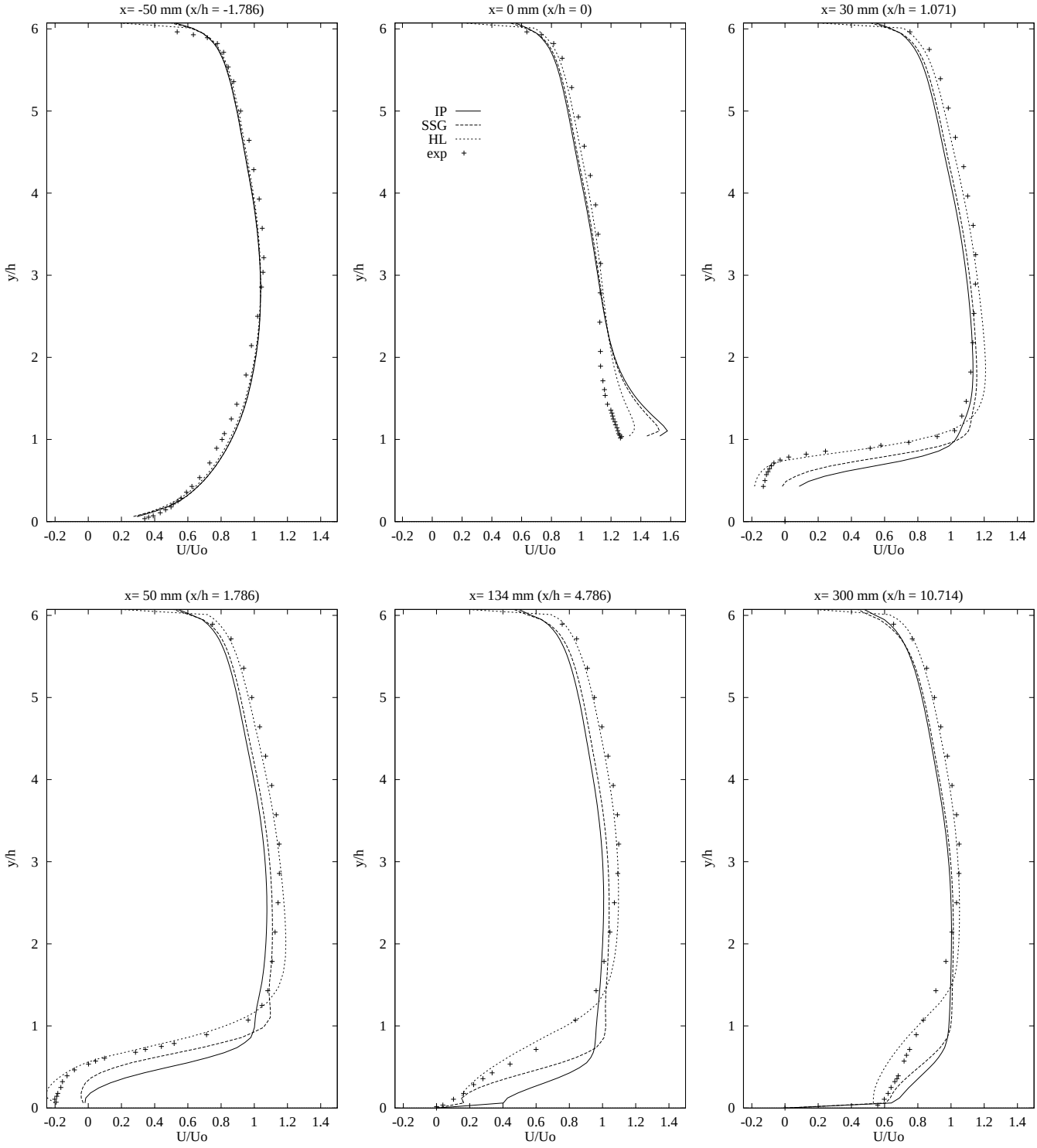

Figure 6.9: *U velocity profiles at some x-locations using RSMs.*

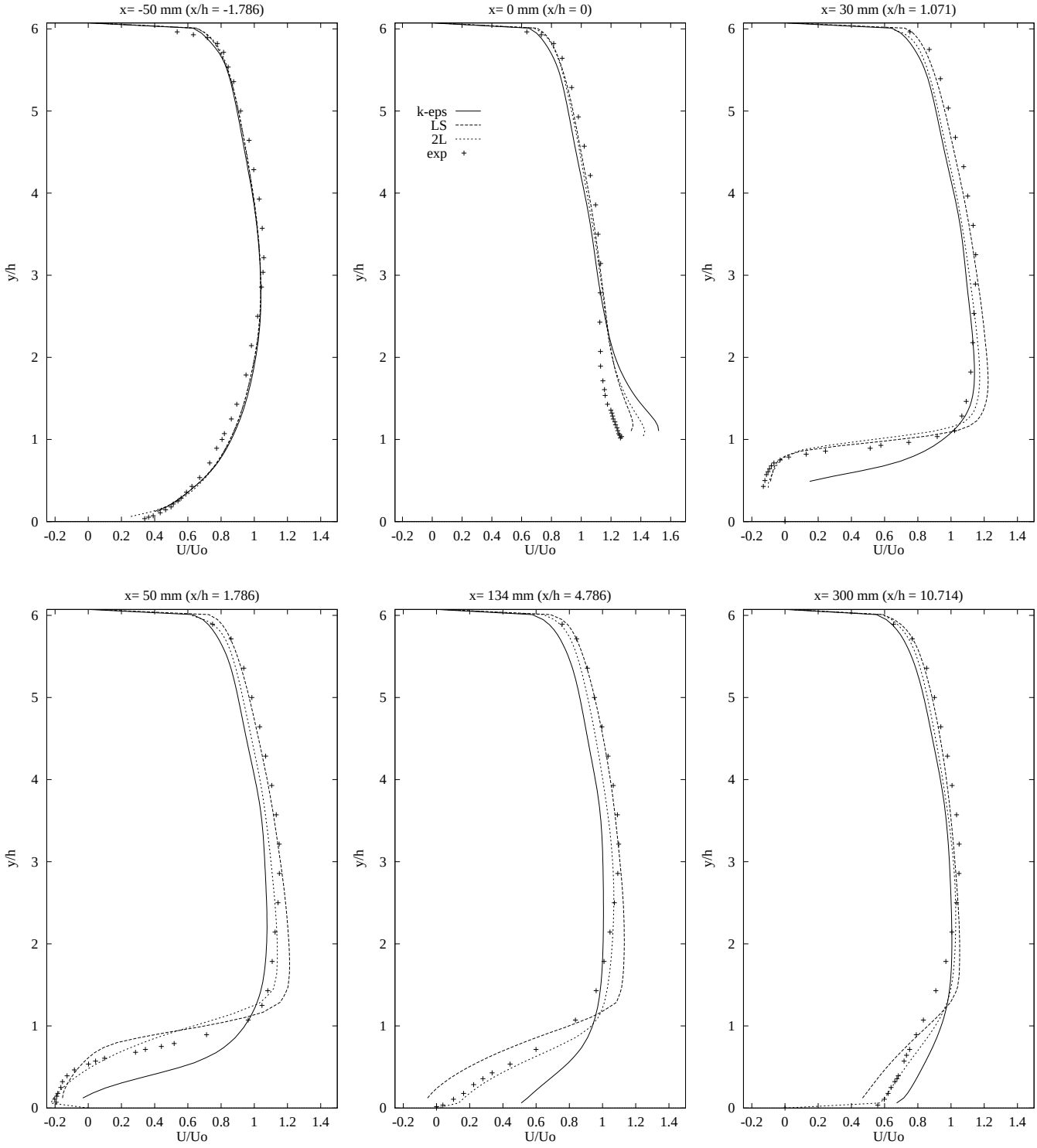

Figure 6.10: *U velocity profiles at some x-locations using EVMs.*

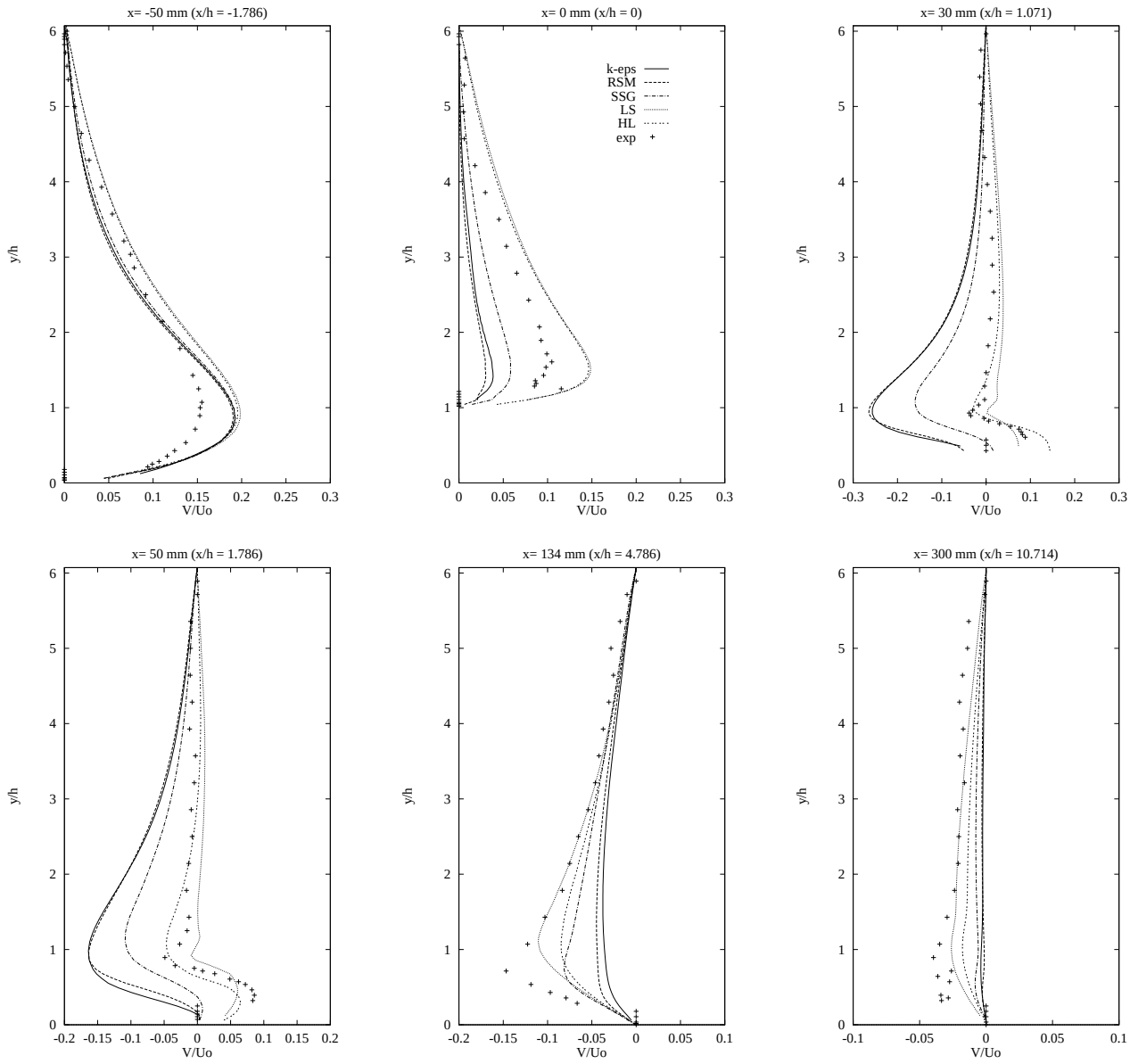

Figure 6.11: *V velocity profiles at some x-locations.*

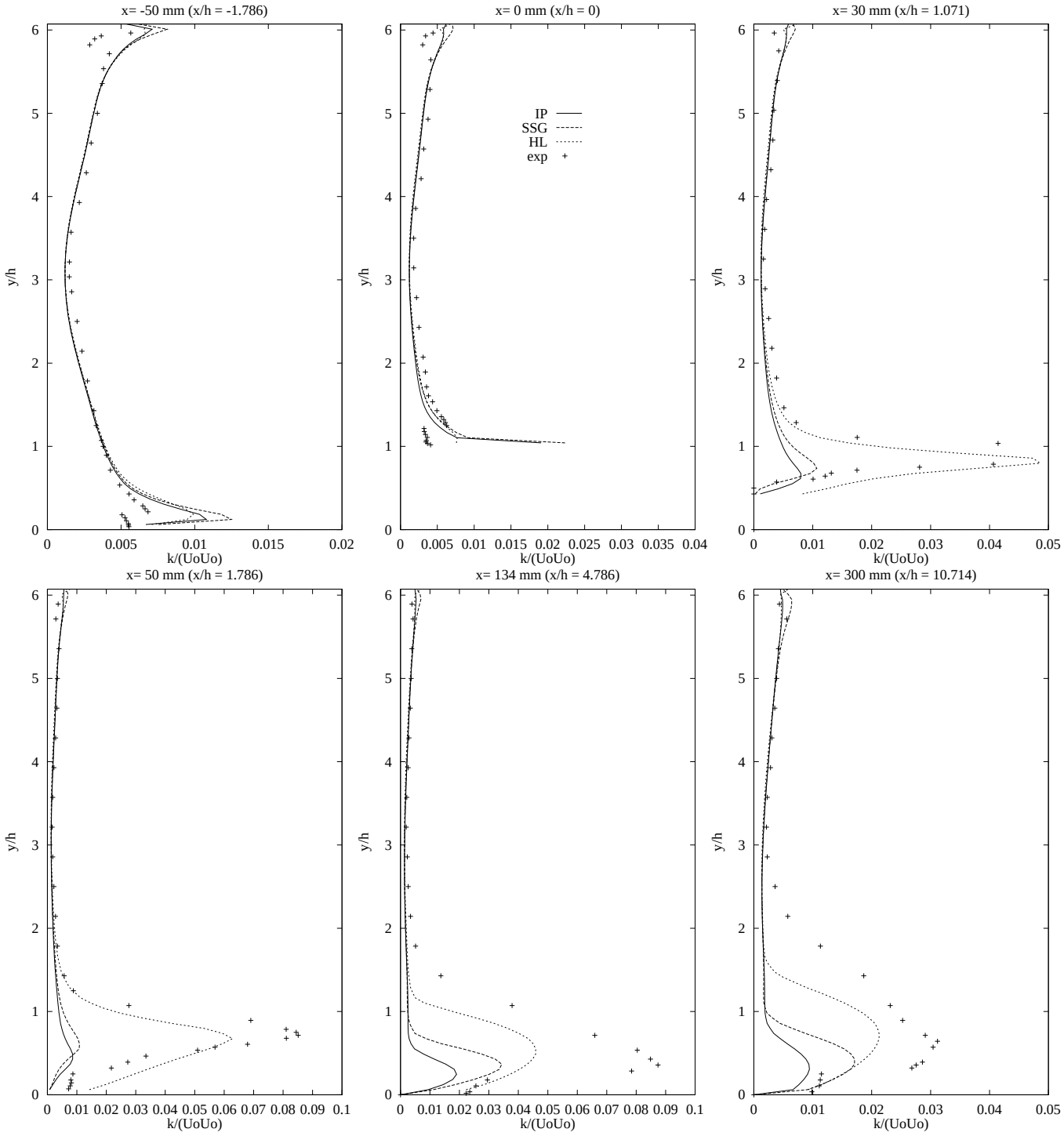

Figure 6.12: *Turbulent kinetic energy profiles, k, at some x-locations using RSMs.*

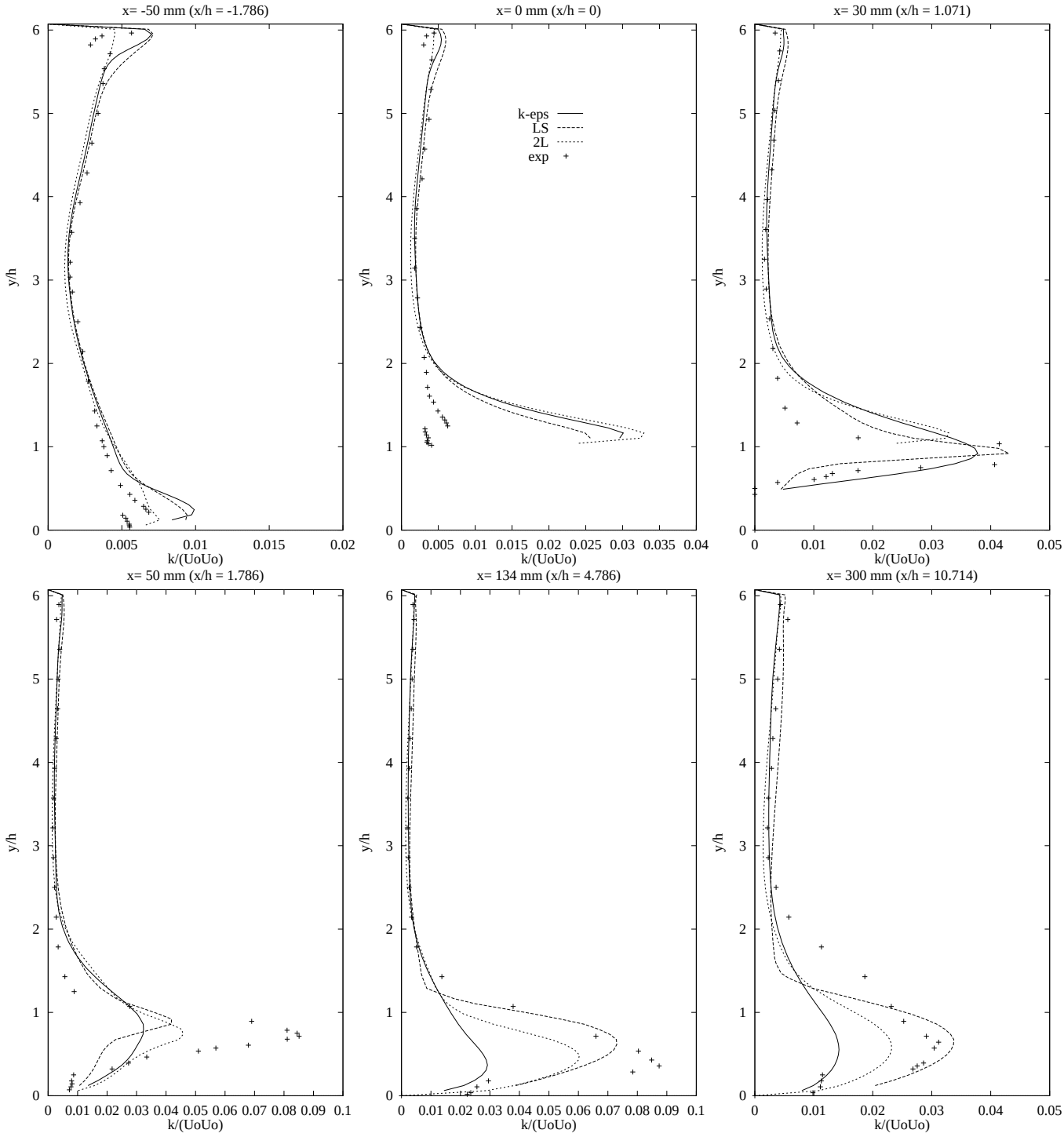

Figure 6.13: *Turbulent kinetic energy profiles, k, at some x-locations using EVMs.*

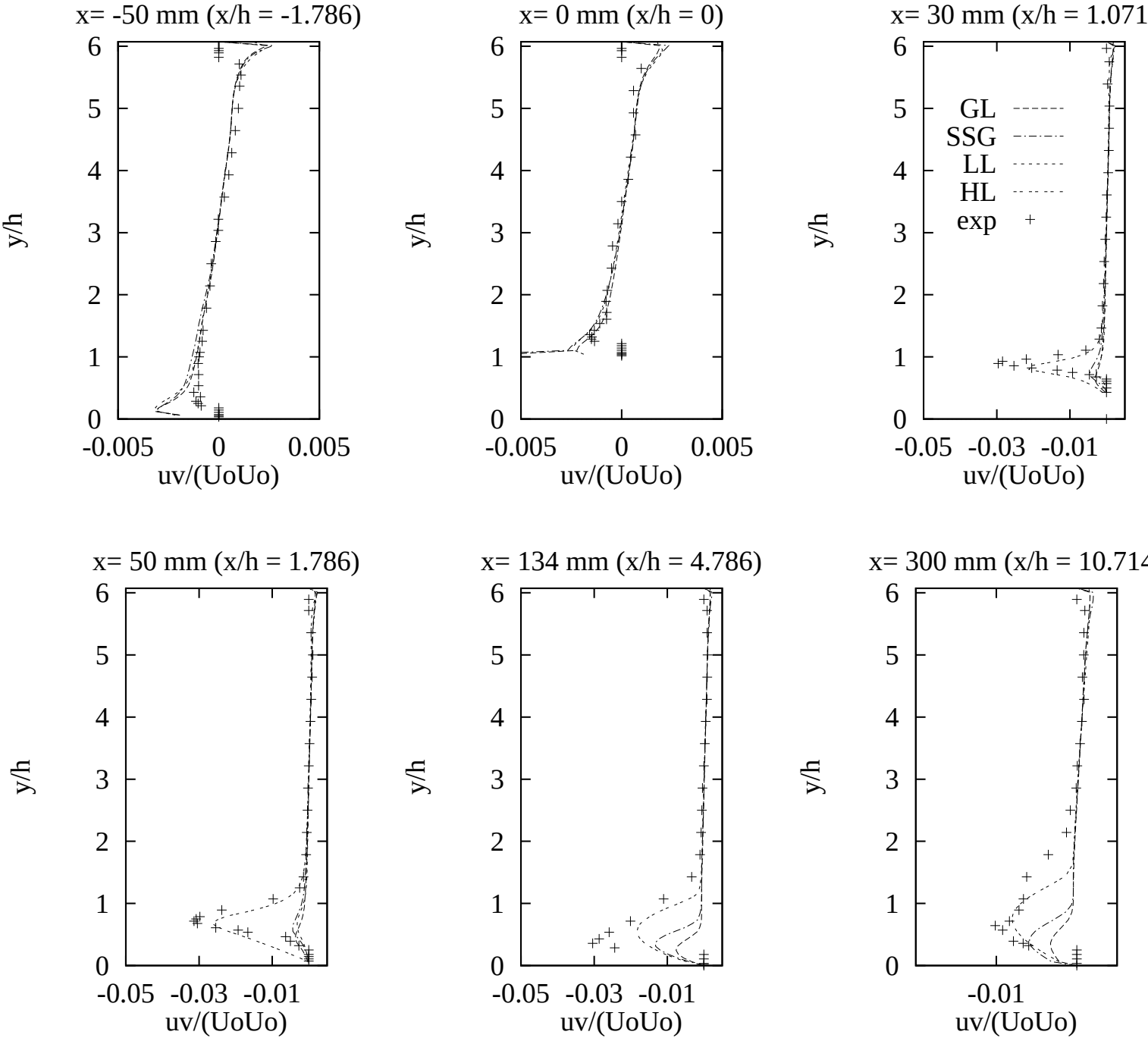

Figure 6.14: *Shear stress profiles, $\overline{uv}$, at some x-locations.*

Chapter 7

Developing flow in curved rectangular duct

The developing flow in a curved, rectangular duct was simulated. Inlet profiles were set from experiments by Kim and Patel [19]. These experiments are also available at several cut planes along the duct.

The test case chosen was one of the test cases in the ERCOFTAC/IAHR *Workshop on Databases and Testing of Calculation Methods for Turbulent Flows*, Chatou 1996, [2], where some of these results were presented.

7.1 Description of the testcase

The computational domain is shown in figure 7.1, and the geometrical data is as follows

- The width of the channel is $h = 20.3$ cm.
- The height of the channel is $B/h = 6$. Using the symmetry condition, the height of the computational domain becomes $b/h = 3$.
- The straight entrance section is $l/h = 4.5$.
- The inner wall radius is $r/h = 3$.
- The duct becomes straight again after the 90-degree bend.
- The straight exit section is $L/h = 25.5$.

A geometric description of the bend is shown in figure 7.1. The experiments by Kim and Patel [19] were made at $x/h = -4.5$, the inlet, immediately before the bend and at 15°, 45° and 75° into the bend. Experiments were also made at two cut planes downstream of the bend, see figure 7.1. The grid used was a one-block mesh with 194 560 cells, see figure 7.2.

7.2 Turbulence models

This test case allowed only for high Reynolds number models to be used because of the severe stability problems encountered using low Reynolds number RSMs.

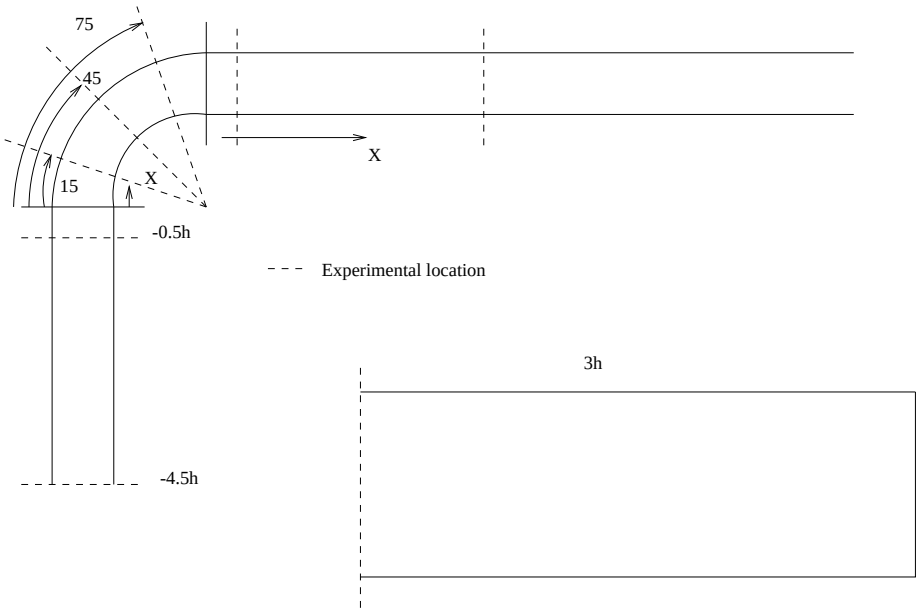

Figure 7.1: *The computational domain for the rectangular duct flow.*

As discussed previously in section 6.6 the HL model was extremely sensitive to underrelaxation parameters, and many iterations were needed to obtain a converged solution. This behaviour became even more pronounced in this 3D test case. Hard underrelaxation seemed to have an effect only on divergence speed with this model. The positive stability effects gained from using the realizable LLI model were tested and resulted in a mix of models referred to as the Present model. This model did show some improvement on numerical stability, but still no converged solution could be obtained on this test case. Thus the models used are:

- The k-ε model.
- The IP model.
- The GL model.
- The LLI model.

7.3 Convection schemes

The higher order upwind scheme is used for mean velocities, the hybrid scheme is used for k , ε and the Reynolds stresses in the differential stress models.

7.4 Results of the simulations of the developing flow in a rectangular duct.

The Reynolds stress models are much more accurate than the k-ε model when simulating the development of the secondary motion, see figure 7.3. Among the stress models, the cubic and realizable LLI model performs best, and mimics the secondary

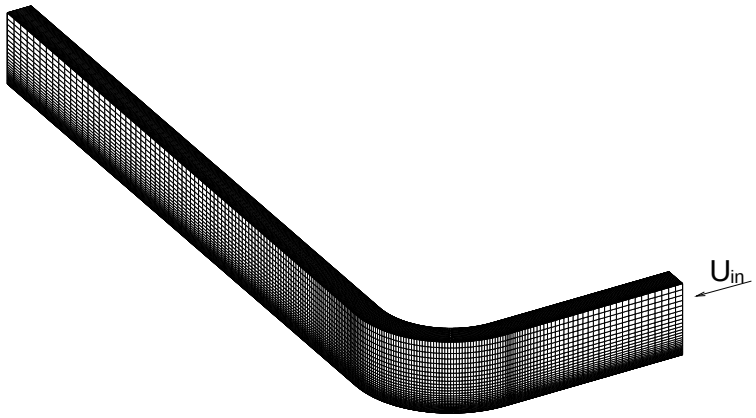

Figure 7.2: *Domain and grid of the bent rectangular duct.*

motion and the turbulence development better than the GL model, see figure 7.5, which in turn performs better than the IP model, even though the wall reflection terms are active only towards the closest wall.

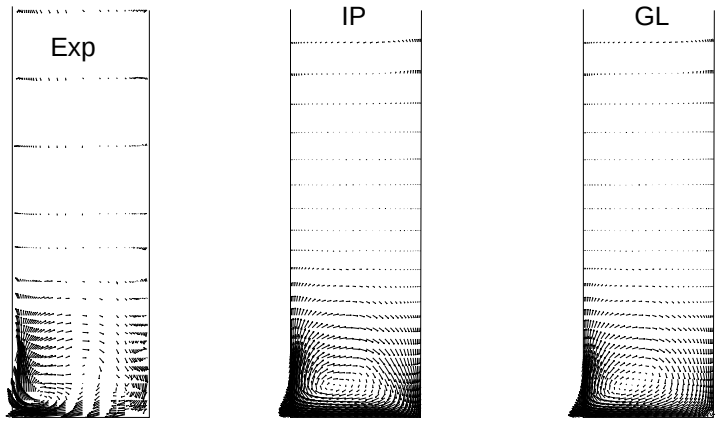

Figure 7.3: *Secondary velocity field at* 45^o *of the bend.*

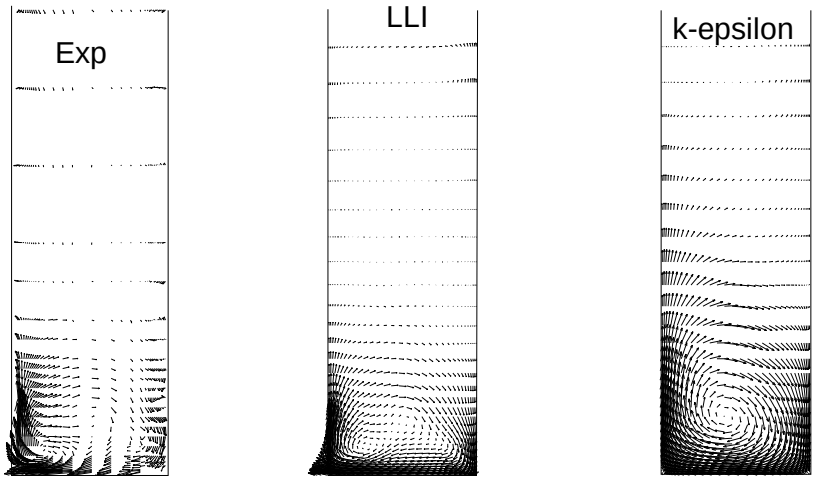

Figure 7.4: *Secondary velocity field at* 45^o *of the bend.*

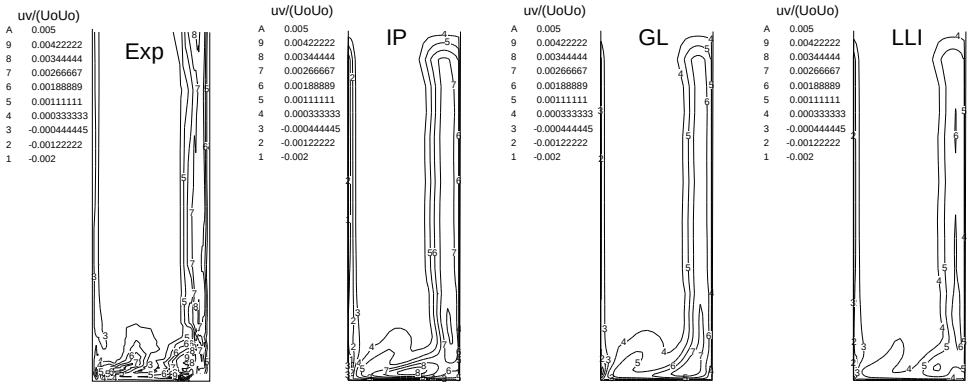

Figure 7.5: *Shear stress, $\overline{uv}$, iso contours at 45^o of the bend.*

Chapter 8

Prolate ellipsoid at incidence

The flow around a 6-to-1 prolate spheroid at incidence was considered. This is one of the best test cases available in which a three-dimensional separation occurs at a curved boundary. The flow pattern is very complex, and it is a delicate task to try to mimic the turbulent structures present with turbulence models. The case has been experimentally documented by several authors, and present computations are compared with experiments by Chesnakas and Simpson [8], Ahn [4] and Kreplin & Stäger [20].

8.1 Description of the test case

The computational domain and mesh are shown in figure 8.1, and the Reynolds number based on the free-stream velocity and the length of the model is $Re_L = 4.2 \cdot 10^6$. The mesh is a 3-block O-type mesh embedded in two blocks upstream and downstream. The number of cells is 326 000. Grid independence was checked using a somewhat finer mesh, and no major difference could be detected.

8.2 Turbulence models

This test case also allowed only for the use of high Reynolds number models owing to severe stability problems that arise when using low Reynolds number RSMs. Thus the models used are the k-ε model, the IP model, the GL model and the LLI model.

8.3 Convection schemes

The higher order upwind scheme is used for mean velocities. The hybrid scheme is used for k , ε and the Reynolds stresses in the differential stress models.

8.4 Results

A three dimensional separation is present in the flow over a 6-to-1 prolate spheroid and the flow structures are very complex. A primary and a secondary vortex are formed when the separation occurs.

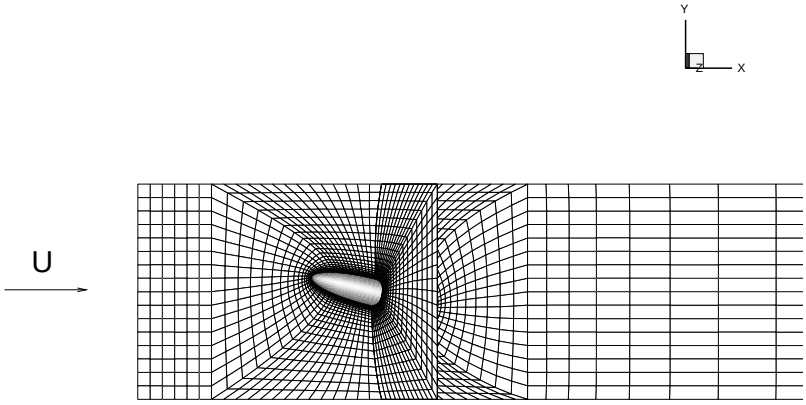

Figure 8.1: *Domain and grid of the 6-to-1 prolate spheroid. The angle of attack is 10 degrees.*

Friction stream traces are shown in figure 8.2. Comparisons are made with experiments by Kreplin & Stäger [20] where the Reynolds number is larger, that is $Re_L = 7.7 \cdot 10^6$. All models separate too late in comparison with experiments, except for the LLI model.

Pressure distributions at walls are available from Ahn's [4] experiments and comparisons with simulations are shown in figure 8.3. Surprisingly enough the k-ε model performs

best even though the separation is poorly predicted by this model.

Velocity profiles compared with the experiments of Chesnakas & Simpson are shown in figure 8.4 and are extracted at $x/L = 0.7622$ in the radial direction of an angle $\beta = 125^{\mathrm{O}}$ from the windward center radius. In the experiments separation at this x location occurs at approximately $\beta_{\mathrm{sep}} = 123^{\mathrm{O}}$. For the U velocity, the cubic LLI model matches experiments best, at least in shape. The k-ε model also gives fairly accurate results for U. For the vertical and spanwise velocity components, all models fail in predicting the proper level, although the shape is more or less correct for all models. Since the main flow is poorly predicted by all models used, the turbulence is naturally not either well predicted, see figure 8.5. Among the models used, the LLI model gives the best overall performance. The model also showed some potential numerically and proved to be the most stable model among the RSMs. This is most likely due to the realizability constraints imposed on the model.

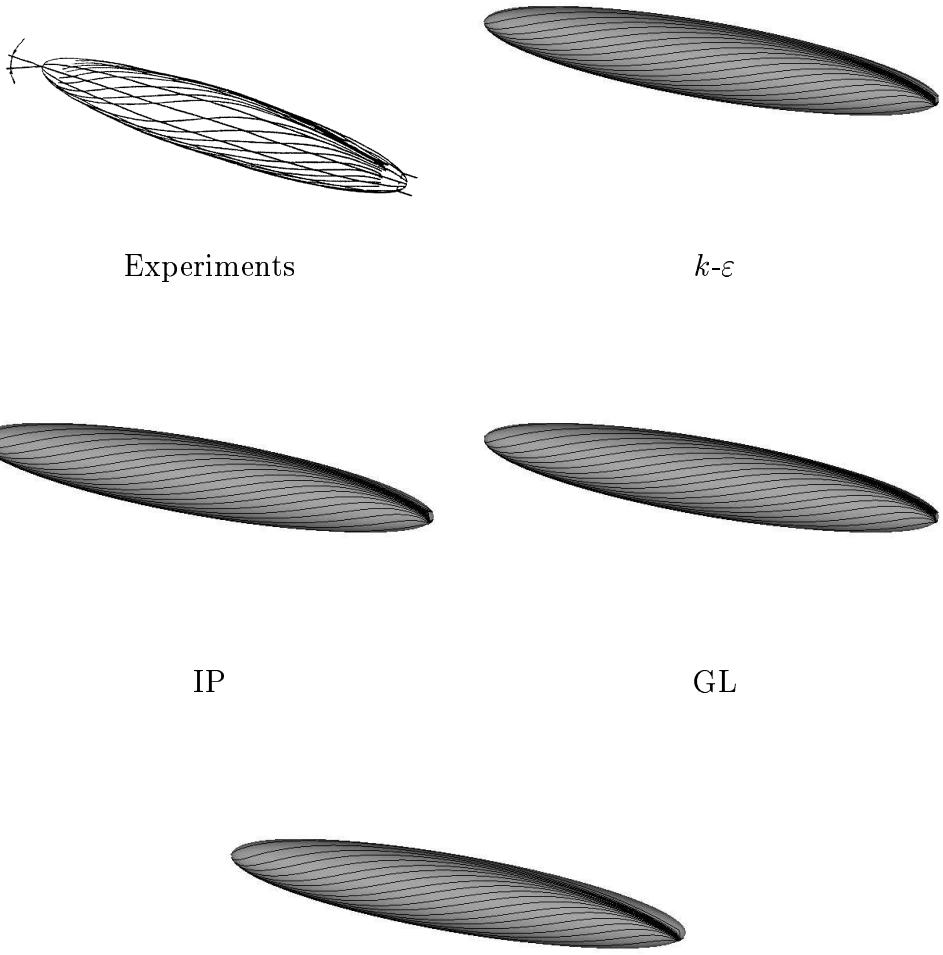

Figure 8.2: *Friction streamtraces on the surface of the body.*

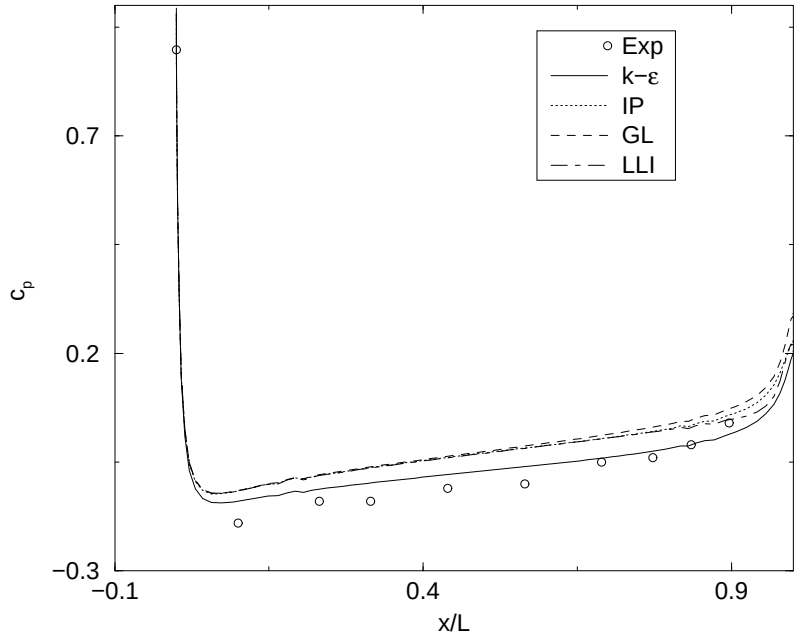

Figure 8.3: *Pressure coefficient at the wall along the symmetry plane on the suction side.*

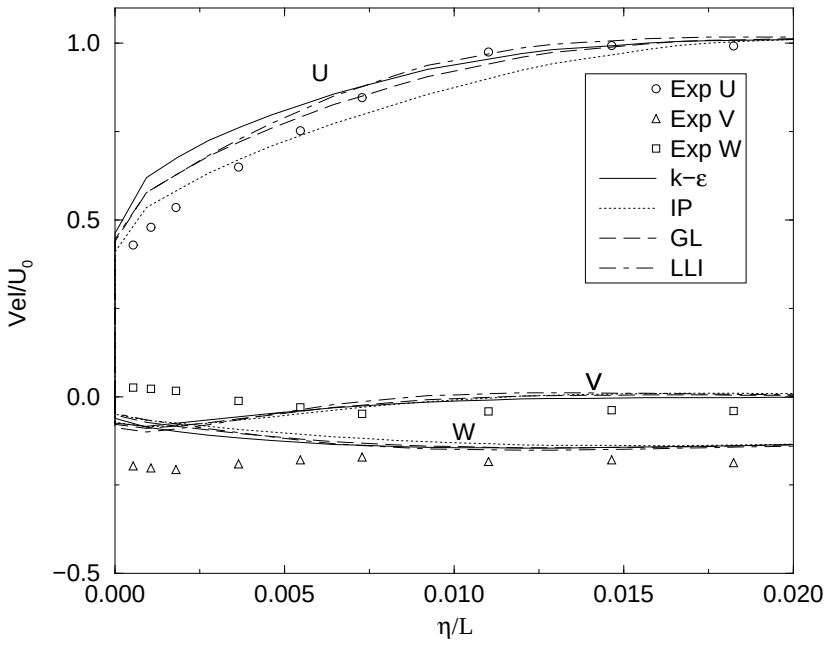

Figure 8.4: *Velocity at x/L=0.7622 as a function of radial distance from the wall, η. The profile is taken at an angle $\beta = 125^o$ from the center windward side radius.*

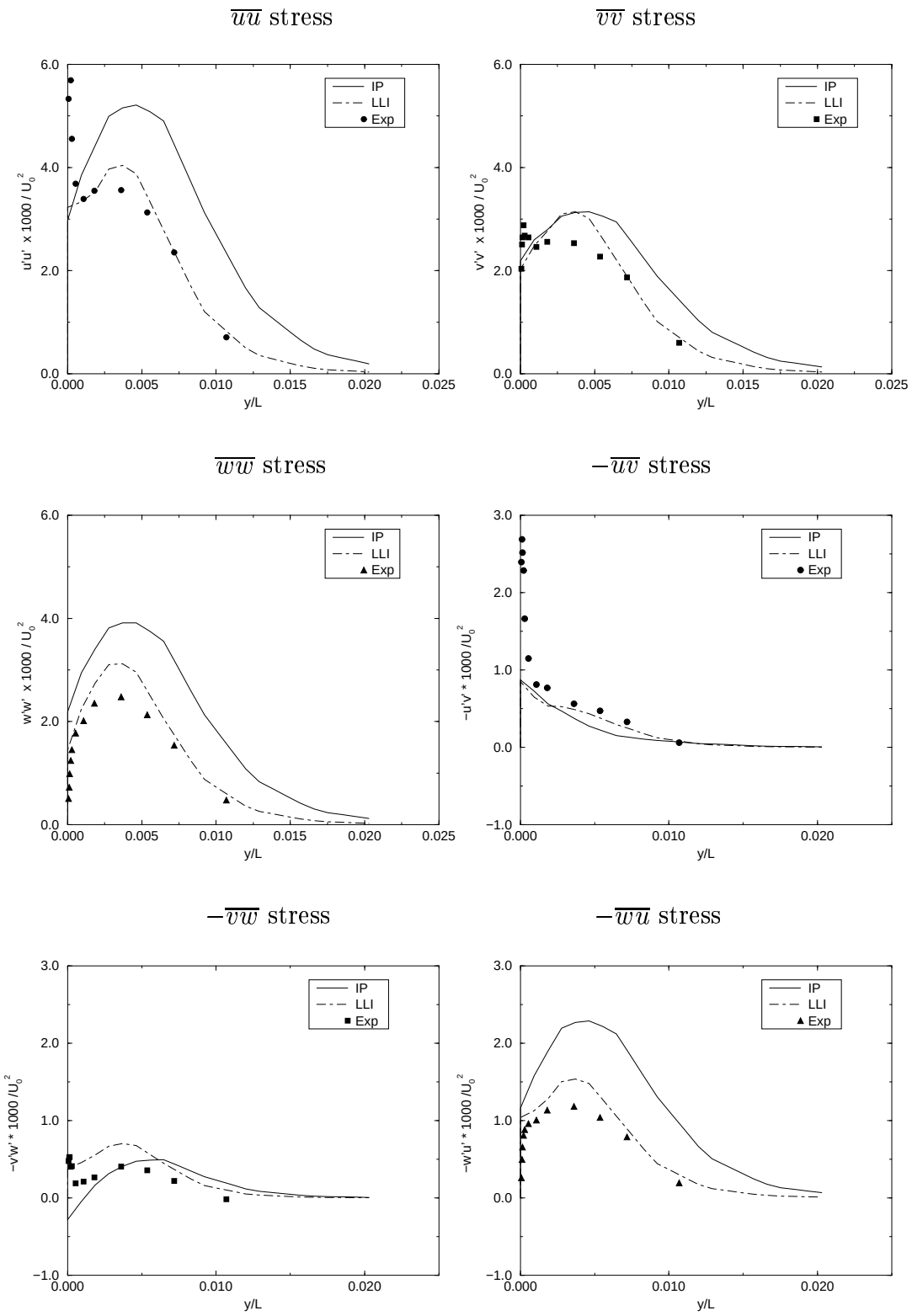

Figure 8.5: *Reynolds stress profiles taken at x/L=0.7622.* $\beta = 125^o$

Bibliography

[1] *4th ERCOFTAC/IAHR Workshop on Refined Flow Modelling*, University of Karlruhe, Germany, 1995.

[2] *5th ERCOFTAC/IAHR Workshop on refined flow modelling*, Electricit'e de France Chatou, France, 1995.

[3] AEA Technology, Harwell Laboratory, UK. *CFDS-FLOW3D 3.3 User Guide*, 1994.

[4] S. AHN. *An experimental study of flow over a 6 to 1 prolate spheroid at incidence.* PhD thesis, Virginia Polytechnic Institute and State Univ., Blacksburg, Virginia, 1992.

[5] M.V. ALMEIDA, D.F.G. DURAU, and M.V. HEITOR. Wake flows behind two-dimensional hills. *Exp. Thermal and Fluid Science*, 7:87, 1993.

[6] T.V. BOUSSINESQ. *Mém. pres Acad. Sci.*, 3rd ed, PARIS XXIII, p.46, 1877.

[7] H.C. CHEN and V.C. PATEL. Near-wall turbulence models for complex flows including separation. *AIAA J.*, 26:641–648, 1988.

[8] C.J. CHESNAKAS and R.L. SIMPSON. Full three-dimensional measurements of the cross-flow separation region of a 6:1 prolate spheroid. *Experiments in Fluids*, 17:68–74, 1994.

[9] M.K. CHUNG, S.W. PARK, and K.C. KIM. Curvature effect on third-order velocity correlations and its model representation. *Phys. Fluids*, 30:626–628, 1987.

[10] T.J. CRAFT. *Second moment modeling of scalar transport.* PhD thesis, dept of Mech Eng, Univ. of Manchester, Faculty of Technology, Manchester, England, UK, 1991.

[11] T.J. CRAFT and B.E. LAUNDER. Improvements in near wall Reynolds stress modelling for complex flow geometries. In *10th Symp. Turbulent Shear Flows*, The Pennsylvania State University, USA, August 1995.

[12] B.J. DALY and F.H. HARLOW. Transport equation in turbulence. *Phys. Fluids*, 13:2634–2649, 1970.

[13] L. DAVIDSON. Prediction of the flow around an airfoil using a Reynolds stress transport model. *ASME J. Fluid Engng.*, 117:50–57, 1995.

[14] L. DAVIDSON. Reynolds stress transport modelling of shock-induced separated flow. *Computers & Fluids*, 24:253–268, 1995.

[15] M.M. GIBSON and B.E. LAUNDER. Ground effects on pressure fluctuations in the atmospheric boundary layer. *J. Fluid Mech.*, 86:491–511, 1978.

[16] M. HALLBÄCK, A. JOHANSSON, D.S. HENNINGSON, and H.P. ALFREDSSON. *Turbulence and transition modelling.* Kluwer Academic Publishers, Dordrecht/Boston/London, 1995.

[17] K. HANJALIĆ and B.E. LAUNDER. Contribution towards a Reynolds-stress closure for low-Reynolds-number turbulence. *J. Fluid Mech.*, 74:593–610, 1976.

[18] T.T. HUANG, H.T. WANG, N. SANTELLI, and N.C. GROVES. Propeller/stern/boundary layer interaction on axisymmetric bodies. theory and experiment. Research and development rept., David W. Taylor Naval Ship Research and Development Center, Ship performance dept., 1976.

[19] W.J. KIM and V.C. PATEL. Origin and decay of longitudinal vortices in developing flow in a curved rectangular duct. *J. Fluids Eng.*, 116:45, 1994.

[20] H.-P. KREPLIN and R. STÄGER. Measurements of the reynolds-stress tensor in the three-dimensional turbulent boundary layer. In *9th Symp Turbulent shear flows*, Kyoto, Japan, 1993.

[21] J. LAUFER. Investigation of turbulent flow in a two-dimensional channel. rept. 1053. Technical report, California Institute of Technology, 1952.

[22] B.E. LAUNDER and S.-P. LI. On the elimination of wall-topography parameters from second-moment closure. *Phys. Fluids*, 6(2):999–1006, 1994.

[23] B.E. LAUNDER, G.J. REECE, and W. RODI. Progress in the development of a Reynolds-stress turbulence closure. *J. Fluid Mech*, 68(3):537–566, 1975.

[24] B.E. LAUNDER and B.T. SHARMA. Application of the energy dissipation model of turbulence to the calculation of flow near a spinning disc. *Lett. Heat and Mass Transfer*, 1:131–138, 1974.

[25] B.E. LAUNDER and D.B. SPALDING. The numerical computation of turbulent flows. *Computer Methods in Applied Mech. and Eng.*, 3:269–289, 1974.

[26] H. LE and P. MOIN. Direct numerical simulation of turbulent flow over a backward facing step. Report NO. TF-58, Stanford University, Dept. Mech. Eng., 1994.

[27] F.S. LIEN and M.A. LESCHZINER. Second-moment modelling of recirculating flow with a non-orthogonal collocated finite volume algorithm. In *8th Symp. Turbulent Shear Flows*, Technical University of Munich, Germany, September 1991.

[28] D. NAOT, A. SHAVIT, and M. WOLFSHTEIN. Interactions between components of the turbulent velocity correlation tensor. *Israel J. Techn.*, 8:259, 1970.

[29] S.B. PARK, M.K. CHUNG, and D.H. CHOI. Reynolds-stress model analysis of turbulent flow over a curved axisymmetric body. *AIAA J.*, 29(4):591–594, 1991.

[30] M. RAMNEFORS, E. HOLMBERG, R. BENSRYD, and S. PERZON. Accuracy of drag predictions on cars using CFD- Effect of grid refinement and turbulence models. In *SAE International Congress & Exposition*, Detroit, USA, 1996.

[31] M. RAMNEFORS, S. PERZON, and L. DAVIDSON. Accuracy in drag predictions on automobiles. In *Vehicle aerodynamics*, Loughborough Univ. of Techn. 18-19 July, UK, 1994.

[32] J.C. ROTTA. Statistische theorie nichthomogener turbulenz. *Zeitschrift für Physik*, 129:547–572, 1951.

[33] C.G. SPEZIALE, S. SARKAR, and T.B. GATSKI. Modelling the pressure-strain correlation of turbulence: an invariant dynamical system approach. *J. Fluid Mech.*, 227:245–272, 1991.

[34] H. TENNEKES and J.L. LUMLEY. *A first course in turbulence.* The MIT Press, Cambridge, Massachusetts, 1972.

[35] M. WOLFSHTEIN. The velocity and temperature distribution in one-dimensional flow with turbulence augmentation and pressure gradient. *Int. J. Mass Heat Transfer*, 12:301–318, 1969.